Materials Horizons

ROYAL SOCIETY OF CHEMISTRY

REVIEW

View Article Online
View Journal | View Issue

Cite this: *Mater. Horiz.*, 2025, **12**, 10453

Disorder by design: unveiling local structure and functional insights in high entropy oxides

John P. Barber,[a] William J. Deary,[a] Andrew N. Titus,[a] Gerald R. Bejger,[a] Saeed S. I. Almishal[b] and Christina M. Rost*[a]

High entropy oxides (HEOs) are a rapidly growing class of compositionally complex ceramics in which configurational disorder is engineered to unlock novel functionality. While average crystallographic symmetry is often retained, local structural and chemical disorder, including cation size and valence mismatch, oxygen sublattice distortions, and site-specific bonding, strongly governs ionic transport, magnetic ordering, and dielectric response. This review outlines how these modes of disorder manifest across key oxide families such as rock salt, spinel, fluorite, and perovskite. We highlight recent advances in spectroscopy, total scattering, and high-resolution microscopy enable multi-scale insight into short- and intermediate-range order. By integrating experimental observations with theoretical modeling of entropy and local energetics, we establish a framework linking structural heterogeneity to emergent properties. These insights not only deepen our fundamental understanding of disorder–property relationships but also offer a path toward rational design of tunable materials for catalysis, energy storage, electronics, and much more.

Received 1st June 2025,
Accepted 28th August 2025

DOI: 10.1039/d5mh01033k

rsc.li/materials-horizons

Wider impact

This review explores how local structural disorder in high entropy oxides (HEOs) can be harnessed as a design principle for tuning functional properties. Traditionally, disorder in ceramics was seen as a challenge to be minimized, but HEOs invert this paradigm by leveraging configurational complexity to unlock new behavior. Recent developments including advances in X-ray absorption spectroscopy, total scattering, electron microscopy, and atom probe tomography have made it possible to characterize short- and intermediate-range order with unprecedented resolution. These tools now allow researchers to connect specific types of disorder, such as sublattice-selective mixing or oxygen vacancy clustering, to changes in ionic conductivity, magnetism, and redox chemistry. This area is of broad significance because many technologically relevant materials including catalysts, solid electrolytes, ferroelectrics, and radiation-tolerant oxides derive their performance from local structure rather than long-range crystallinity. The concepts developed through HEOs are therefore relevant to a wide spectrum of materials systems. Looking ahead, the integration of multi-modal characterization with theory and data-driven design will transform how we understand and exploit disorder. This review outlines a roadmap for doing so, establishing local structure as a foundational lever for materials discovery across disciplines including energy storage, computing, and extreme environment technologies.

1. Introduction

The ability to synthetically manipulate materials now surpasses what occurs in nature, down to the atomic scale. Properties central to modern technologies are ultimately rooted in a material's structure and chemistry.[1] If structure governs the available physical properties, then composition determines their magnitude. Even within a single crystal family, such as perovskites, sub-angstrom displacements can dictate whether a material is ferroelectric or paraelectric, underscoring the critical role of local structure in designing functionality. The interplay of multiple species can further enhance material performance; for example, early n-type doping of silicon with phosphorus increased its electron mobility threefold.[2,3] High entropy oxides (HEOs) extend these concepts by introducing extreme cation disorder within a crystalline framework, often maintaining high symmetry despite chemical complexity. This disorder leads to locally distinct environments that disrupt long-range periodicity, while configurational entropy expands the solubility limits of constituent elements.[4] Together, these attributes enable access to novel compositions and potentially emergent properties, making HEOs highly tunable and synthetically versatile.

The unique combination of disorder and symmetry has fueled rapid interest in HEOs, and several excellent reviews

[a] *Department of Materials Science and Engineering, Virginia Polytechnic Institute and State University, Blacksburg, Virginia 24061, USA. E-mail: cmrost@vt.edu*
[b] *Department of Materials Science and Engineering, The Pennsylvania State University, University Park, Pennsylvania 16802, USA*

have preceded this one. Early articles focused on high entropy alloys and ceramics more broadly,[5–7] while subsequent reviews refined the scope. Musicó *et al.* provided an overview of high entropy oxides in 2020,[8] Brahlek *et al.* proposed definitions for the field in 2022,[9] and Kotsonis *et al.* linked compositional disorder with functional response.[4] Rost *et al.* offered an

John P. Barber

John Barber received a BS in Physics with minors in Materials Science and Mathematics from James Madison University. He is now pursuing a PhD in Materials Science and Engineering at Virginia Tech while doing research for Dr. Christina Rost. His research focuses on the fabrication of ceramic thin films for pyroelectric -based sensing and exploring the local structure of HEO compositions.

William J. Deary

William Deary is an undergraduate researcher working with Dr. Christina Rost at Virginia Tech. He earned an A. S. in Engineering from Northern Virginia Community College in August 2023 and will complete his BS in Materials Science and Engineering in December 2025, where he plans to continue toward a PhD. His research focuses on high entropy oxides and their functional properties. He is enthusiastic about advancing the understanding of these materials and their applications, with a strong interest in how milling and particle size can be an avenue for tailoring material properties.

Andrew N. Titus

Andrew Titus is an undergraduate researcher working with Dr. Christina Rost at Virginia Tech. He will complete his BS in Materials Science and Engineering at Virginia Tech in May 2027. Andrew's research focuses on powder processing of high entropy spinels and the synthesis and integration of thin film oxides for pyroelectric applications.

Gerald R. Bejger

Gerald (Jerry) Bejger is a PhD candidate at Virginia Tech under the direction of Dr. Christina Rost. He received a BS in Physics from James Madison University in 2023. Jerry's research interests include local and electronic structure of complex oxides including high entropy and amorphous systems.

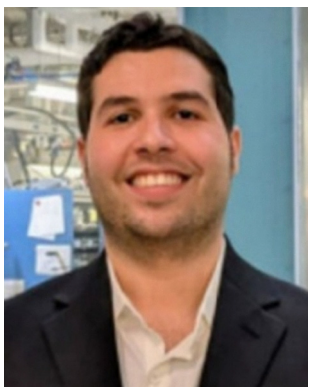

Saeed S. I. Almishal

Dr Saeed Almishal completed his PhD in Materials Science and Engineering at The Pennsylvania State University in 2024. Now a research professor at Penn State, he investigates the thermodynamics, synthesis, and emergent properties of novel disordered materials and high-entropy oxides in bulk and thin films.

Christina M. Rost

Dr Christina (Tina) Rost is an Assistant Professor of Materials Science and Engineering at Virginia Tech. Her research focuses on leveraging disorder to develop materials with tunable properties for advanced technologies. Dr Rost earned a PhD in Materials Science and Engineering from North Carolina State University in 2016, where she helped pioneer the field of high-entropy ceramics. She is the recipient of an NSF CAREER Award, the ACerS Basic Sciences Division Early Discovery Award, and the Provost's Award for Excellence in Research and Scholarship at James Madison University.

editorial update on recent breakthroughs that continue to expand the relevance of high entropy materials.[10]

Nature offers inspiration for such complexity as minerals exhibit remarkable chemical and structural richness, with the most complex known mineral incorporating H, C, O, Mg, Ca, and U into a tetragonal lattice.[11,12] Yet HEOs are distinct: they are synthetically designed to achieve high symmetry with extensive elemental solubility, guided by, but not constrained to, natural principles.[13–15] The first reported ''HEO'', as the community has come to accept them, $(MgCoNiCuZn)_{0.2}O$ (often referred to as ''J14''), was synthesized as a rock salt structure in 2015.[16] Since then, the concept has expanded across numerous chemistries and crystallographic systems. The review on high entropy ceramics by Xiang *et al.* provides a comprehensive list of the crystal systems that were successfully synthesized as high entropy compositions as of 2021.[6] Oxygen, boron, silicon, and some amounts of phosphorous, fluorine, or tellurium have been used as anions. Within the regular oxide space, rock salt, fluorite, pyrochlore, perovskite, spinel, magnetoplumbite, garnet, and dual-phase systems have been created.

Though discovered nearly a decade ago, HEOs potentially rival state-of-the-art materials in several applications. From rechargeable batteries[17] to hydrogen storage,[18] hydrogen evolution,[19] oxygen catalysis,[20] and supercapacitors;[21] high entropy compositions hold a promising future for functional materials. Fig. 1 depicts a concept co-occurrence network for HEOs and synonymous materials in combination with the trends in yearly publication rates beginning with the seminal paper.[16] HEOs are of clear interest to the ceramics community. While emerging properties are still the end goal, a closer look at the local length scales in these highly disordered systems is becoming more and more necessary.

This review focuses specifically on the local structural environments in HEOs following a short review of the basics: how they arise, some of the more common characterization techniques used to ascertain structure, and examples of their implications for material property performance. We begin with foundational definitions and structural motifs, followed by a discussion of disorder and its influence on physical properties. We then summarize key characterization tools capable of probing local structure, before concluding with case studies that highlight how structural insights are informing function—and where opportunities remain for future progress.

2. Foundational concepts

2.1 Terminology and definitions

It is important to distinguish high entropy oxides (HEOs) from compositionally complex oxides (CCOs) and entropy-stabilized oxides (ESOs). As discussed in the review by Brahlek *et al.*,[9] CCOs represent the broadest category of disordered oxides and are defined as materials containing more constituent elements than their parent compositions. HEOs are a subset of CCOs, typically consisting of five or more elements in (approximately) equimolar ratios randomly dispersed across a single crystallographic site, resulting in increased configurational entropy. ESOs, in contrast, are a thermodynamic subset of HEOs where the entropy contribution is large enough to overcome a system's positive enthalpy at high temperatures, thus stabilizing a single-phase structure that would otherwise be unfavorable. Such materials are inherently metastable.

While these classifications overlap, they carry important distinctions. ''High entropy'' specifically refers to the configurational entropy of a system. For an ideal system with equimolar occupation of a single sublattice, the configurational entropy can be calculated as $S_{config} = R\ln(n)$ where R is the ideal gas constant and n is the number of elements on the site.[15] For five equimolar constituents, the ideal configurational entropy will be $1.609R$. High entropy alloys are typically defined as having at least five components in proportions $5\% \leq \text{mol}\% \leq 35\%$ or having a configurational entropy above $1.5R$ (J K) mol^{-1}.[22,23] This definition is often extended to classify HEOs.

The defining feature of ESOs is that their positive enthalpy of formation is counteracted by a sufficiently negative entropy term at high temperature, enabling stabilization of a single phase. An illustration depicting the relationships between classifications is shown in Fig. 2. Rost *et al.* outlined four experimental criteria to demonstrate that $(MgCoNiCuZn)_{0.2}O$ is an ESO.[16] They observed a reversible phase transition: a pure rock salt phase precipitated CuO upon slow cooling to 750 °C but reverted to a single-phase rock salt structure upon reheating to 1000 °C. Varying the molar ratios of cations revealed that the minimum single-phase formation temperature (875 °C) occurred at equimolar composition. Then, differential scanning calorimetry and thermogravimetric analysis confirmed an endothermic transformation, indicating that entropy drives the solid-state reaction.[24] Finally, extended X-ray absorption fine structure (EXAFS) and scanning transmission electron microscopy with energy-dispersive X-ray spectroscopy (STEM-EDS) confirmed a homogeneous cation distribution at both the local and nanometer scales.[16]

2.2 Thermodynamic framework

The most common and straight forward way that high entropy systems are explained is by means of free energy relationships. Relative phase stability can be predicted by the Gibbs free energy, $\Delta G(T,P) = \Delta H(T,P) - T\Delta S(T,P)$, where ΔG is the change in Gibbs free energy (J mol^{-1}), ΔH is the change in enthalpy (J mol^{-1}), T is the temperature (K), ΔS is the change in entropy ((J K) mol^{-1}), and P is pressure (Pa). Gibbs free energy is a measure of the change in free energy of the system resulting from a process and, consequently, can predict how the system will react. The second law of thermodynamics tells us that a system will be at equilibrium when the free energy is minimized. Therefore, the Gibbs free energy equation can be used to determine the stability of a system.

In an ideal solution, the entropy of mixing is shown by a variation of Boltzmann's law, $\Delta S_{mix} = -R\sum_{i=1}^{N} x_i \ln(x_i)$, where R is the ideal gas constant, x_i is the molar fraction of component

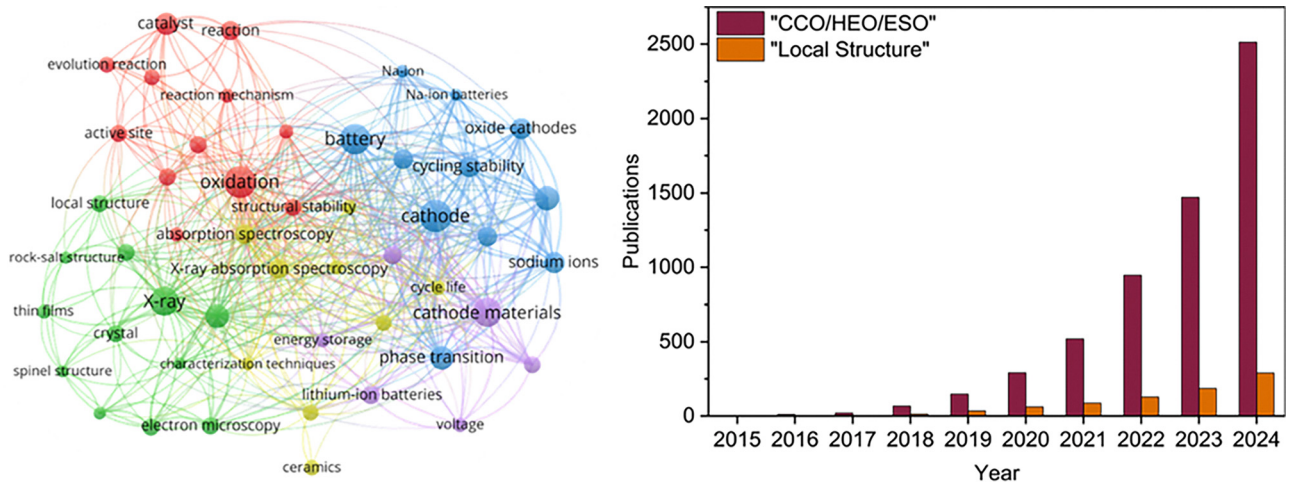

Fig. 1 Concept co-occurrence network and publication trend analysis for high entropy oxide-related materials research. (Left) A concept co-occurrence map generated from literature on compositionally complex, high entropy, and entropy stabilized oxides. Node size reflects term frequency and line thickness indicated co-occurrence strength. Color-coded clusters represent thematically related research ideas, including redox chemistry (red), phase/structure characterization (green/yellow), and cathode development (blue/purple). (Right) Annual publication trends from 2015 to 2024 for two key concept searches: ''compositionally complex/high-entropy/entropy-stabilized oxides'' and ''local structure''.

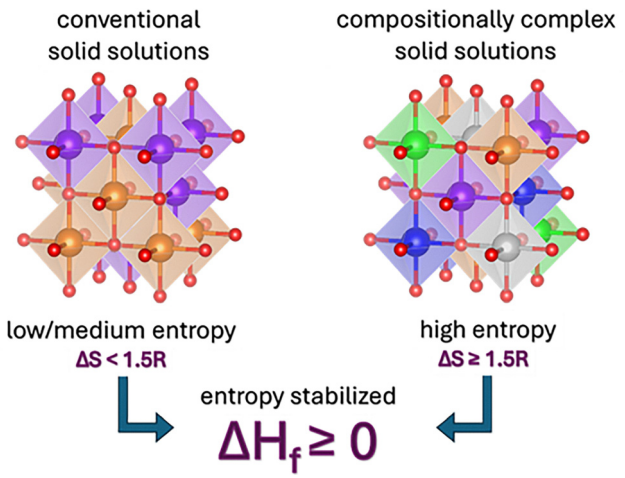

Fig. 2 Simple diagram illustrating relationship between conventional and compositionally complex solid solutions. By convention, a composition is considered high entropy when the number of cation species enables $\Delta S \geq 1.5R$. Both compositionally complex and conventional solid solutions can be entropy stabilized if the enthalpy of formation is positive.

i, and N is the total number of components.[25] From this equation, it can be shown that maximum entropy of mixing can be achieved when the molar fractions are equal.

The enthalpy term arises in regular solutions as there is no heat associated with mixing in ideal solutions.[25] It is given in the equation $\Delta H_{\text{mix}} = \sum_{i,j=1}^{N} a_0 x_i x_j$, where x_i and x_j are the mole fraction of each component in a system with N combinations of components and a_0 is a constant representing the bonding preference between the constituent components. a_0 is unique to each combination of components x_i and x_j and will be positive if chemical separation is preferred and negative if alloys or intermetallic phases are preferred.[25] Substituting equations for ΔS_{mix} and ΔH_{mix} yields a more thorough equation for Gibbs free energy, $\Delta G_{\text{mix}} = \sum_{i,j=1}^{N} a_0 x_i x_j - RT \sum_{i=1}^{N} x_i \ln(x_i)$. This equation fails to account for the fact that both enthalpy and entropy are functions of temperature and pressure, as shown before. Equations for entropy and enthalpy as functions of temperature, given that pressure is typically held constant, can be simplified to, $S(T) = S_0 + C_{\text{P}} \cdot \ln\left(\frac{T}{T_0}\right)$ and $H(T) = C_{\text{P}}T$, respectively, where S_0 is the entropy at temperature T_0 and C_{P} is the heat capacity at constant pressure.[25] When these values are plotted against Gibbs free energy, it is apparent that enthalpy dominates over entropy at low temperatures but, above a sufficient temperature, entropy becomes the dominating term.

$\left(\frac{\delta G'}{\delta n_i}\right)_{T,P,n_j} = \mu_i$ tells us that the chemical potential of a component is equivalent to the partial molal free energy for the component.[25] The chemical potential of a component will determine the mixing equilibrium in a solution and is related to the activity of that component.[15] The change in chemical potential due to mixing is $\Delta\mu_i = R\ln(X_i) + R\ln(\gamma_i)$, wherein γ_i is the activity of the component in solution. The $R\ln(\gamma_i)$ term represents excess chemical potential stemming from the non-ideal mixing and dictates the effects of adding the component to the solution. Many partial enthalpy and partial excess entropy terms arising from different physical aspects, such as surface and magnetic effects, contribute to the excess chemical potential.[15] This tells us that non-ideal contributions to the potential gradient will have an outsized effect as there are more components intermixing in the solution.[15]

2.3 Disorder in oxides

Entropy is traditionally thought of as the level of disorder in a system. While this is not incorrect, it is important to define

what disorder means in the context of HEOs and think about how that produces the elevated entropy in these materials. In crystalline solids, there is no such thing as a perfect crystal, even with stoichiometrically accurate components and ideal conditions. This is due to the tendency for defects to form in order to lower the free energy of the system. In oxides, the formation of these defects is dependent on temperature, composition, and oxygen partial pressure.[26]

Intrinsic defects will form as temperature increases solely due to temperature's negative contribution to the free energy.[27] Defects in crystalline materials range in dimensionality from zero to three—point, line, planar, and volume defects. Intrinsic ionic defects manifest as point defects. Substitutional disorder is when an ion of the formal composition is substituted with another at some fraction of the sites. This can be expanded to chemical disorder if the ions across a sublattice are non-uniform. This distribution of ions will in turn lead to charge disorder as the electronic configuration varies from site to site. Increased competition for local equilibrium will also lead to the formation of point defects, which can be defined as local deviations from the long-range symmetry of the material at a single or pair of lattice sites. These can be vacancies, interstitials, Frenkel[28] and Schottky[29] pairs, or anti-site substitutions.

Differing electronic configurations inherently leads to varying bonding preferences, which in turn contribute to structural disorder. These deviations from ideal symmetry arise as ions adopt new equilibrium positions not dictated by the global periodic lattice. The resulting distortions span a range of length scales—from sub-angstrom displacements to intermediate-range order extending up to $\sim$20 Å.[30] In studies of glasses and amorphous systems, short-range order is often divided into two categories that are also applicable to HEOs: (i) the local structural unit, and (ii) the interconnection between neighboring units.[31] In this review, we use "local structure" to refer to the former, and "short-range order" (SRO) to the latter. Jahn–Teller (J–T) distortions are a common form of local ordering in transition metal oxides.

A prominent example of local ordering in transition metal oxides is the Jahn–Teller (J–T) distortion, which involves the elongation or compression of the ligand coordination environment to lift orbital degeneracy.[32] These distortions, typically observed in ions with degenerate d-electron configurations,[33] can drive local symmetry breaking and lead to SRO depending on the population and distribution of J–T active species in the lattice.

In high entropy oxide systems, disorder emerges as a natural consequence of the thermodynamic and kinetic constraints involved in stabilizing multiple cations within a single crystallographic framework. The random distribution of chemically and electronically dissimilar elements leads to several coexisting types of disorder, including configurational, charge,[34] strain and bond-length disorder.[35] Configurational disorder stems from the stochastic occupation of lattice sites by cations with varying size and valence, while charge disorder arises due to aliovalent substitutions and local charge compensation. Size mismatch among cations introduces local strain fields and lattice distortions, often accommodated through bond angle bending or polyhedral tilting. These distortions may be static or dynamic and can couple to oxygen sublattice rearrangements,[36] further amplifying structural complexity. Collectively, these types of disorder are interdependent and span multiple length scales—from atomic coordination to mesoscale strain—and are central to the emergent functional properties observed in HEOs.

The unusual behaviors of HEOs stem directly from this intrinsic disorder—arising from the random distribution of multiple cation species across a single lattice site and the local equilibria required to maintain charge neutrality. This disruption of bonding networks and electronic environments is the fundamental driver behind many of the characteristic phenomena observed in these materials.

2.4 High entropy effects

There are four widely accepted characteristics of high entropy materials: high entropy, slow kinetics, severe lattice distortion, and a cocktail effect.[37] Research over the past two decades on high entropy materials has revealed additional defining characteristics, including enhanced stability in higher symmetry structures arising from a broad basin of attraction,[38,39] structural evolution,[40] progressive local structure maturation,[41] and diverse functional valence environments.[42,43] Fig. 3 summarizes the key topics of this section—namely the extent to which the classical characteristics can be applied to HEOs and phenomena unique to ceramic systems.

2.4.1 High entropy effect

The mechanisms that lead to high entropy have been defined, but now the effect it has on the material can be discussed. HEOs contain more components on their cation sublattice than traditional oxides. The high configurational entropy induced by the chemical disorder on one (or more) sites of the compound allows for new compositional space to be explored. Typically, this is achieved through incorporating many constituent elements into the material. However, it has been shown that entropy stabilization can occur when the configurational disorder on the cation lattice alone does not reach the $1.5R$ (J K) mol^{-1} threshold. An oxide was synthesized that only had $1.24R$ (J K) mol^{-1} of entropy when considering the cation sublattice, but was stabilized due to vacancies on the oxygen sublattice increasing the configurational entropy.[44] There has been work done in chemically disordering the anion sublattice as well,[45–53] but this departs from the realm of oxides and is therefore omitted from this review.

In high entropy alloys, there have been arguments against configurational entropy being the true force behind the single-phase stabilization of these materials.[7,54,55] Citing the lack of single-phase chemical homogeneity observed in materials many element alloys, the varying enthalpies for intermetallic phases, and loss of single-phase nature when replacing select elements; there is a valid argument to be made. However, there are computational and experimental studies that display entropy being the driving factor in phase stability in high entropy materials, highlighting the necessity of high temperatures in the synthesis to scale the entropic contribution.[16,56–58]

2.4.2 Severe lattice distortion. A consequence of substituting differing atomic radii across a lattice site will result in

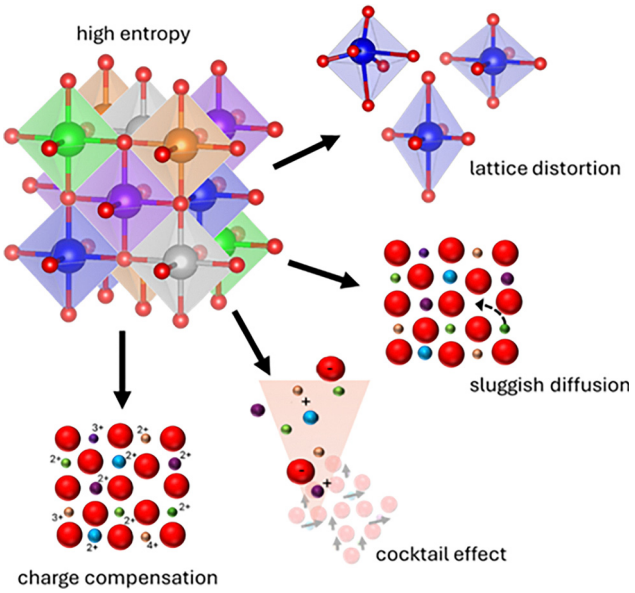

Fig. 3 "4+1" core effects in high entropy oxides. The phases stabilized through high configurational entropy exhibit properties that arise from the many unique combinations of local lattice distortions and charge compensation. In turn, characteristics such as sluggish diffusion and cocktail effects may be present.

anisotropic bond lengths within the material. This impacts more that the structure alone, as Guan *et al.* demonstrated that the shortening of metal–oxygen bonds in a high entropy spinel led to improved stability and performance in catalytic applications.[35] $(MgCoNiCuZn)_{0.2}O$ contains an near-ideal cation matrix, with structural compensation occurring through distortions existing on the oxygen sublattice using EXAFS measurements which agreed with density functional theory (DFT) calculations.[59] Octahedrally coordinated Cu is J–T active and, as such, results in additional lattice distortions around Cu populated sites.[60–62] Rák *et al.* found that Cu being in the rock salt structure resulted in an abnormally high proportion of J–T compression, as opposed to J–T elongation, possibly due to structural competition between elongation preferred by Cu and octahedral structures preferred by the other cations in the lattice.[63]

2.4.3 Sluggish diffusion. The driving force for diffusion is directly related to the chemical potential gradient.[64] The homogenous distribution of cations in HEOs results in an average chemical potential gradient that is flatter than would occur in conventional oxides, reducing the drive for mass transport. While the average potential gradient is flatter, there is still the opportunity for local deviations to be large and form 'traps' for migrating ions. Lattice distortions, misaligned lattice sites, and different ionic radii create physical barriers that can stunt the movement of ions, contributing to slow diffusion. Slow diffusion characteristics of HEOs are observed in mechanisms like vacancy migration, interstitial diffusion, and grain growth. In a high entropy environment, the creation and movement of cation vacancies is often more complex due to the diversity of electronegativity and atomic radius of the constituent elements. Interstitial diffusion is stunted in HEOs as the diverse potential landscape limits the number of suitable interstitial sites and increases the activation energy for diffusion.[65] Sluggish diffusion effects have been observed in the reduction of grain growth rates as well,[66] which can be beneficial in high temperature applications.[67] It is important to note that the concept of sluggish diffusion being an intrinsic characteristic of high entropy materials has been contested, especially in alloys where fundamental diffusion studies are more prevalent.[68–71]

Dąbrowa *et al.* surmises that the inclusion of Mn in the original HEA was the basis for the idea that sluggish diffusion is inherent to the high entropy compositions.[68] Their tracer diffusivity studies on alloys of varying composition showed that the inclusion of Mn led to the observation of this sluggish diffusion. The review on the topic of sluggish diffusion in HEAs by Divinski *et al.* discusses the shortcomings of methods and interpretations of early studies, dictating that the observed phenomena arise from local atomic interactions and correlation effects.[70] Grzesik *et al.* performed studies on the defects and transport properties in two HEO compositions.[72,73] It was found that the chemical diffusion coefficient evolves with pO_2 due to complex defect structures, with the spinel composition exhibiting a reduction by two orders of magnitude with decreased pO_2. Ultimately values were within the range of traditional metal oxides, indicating that sluggish diffusion may be a misnomer in HEOs as well.

2.4.4 Cocktail effects

The cocktail effect is something that is not well understood but is observed *via* the unexpected properties that arise. It is best described as the synergistic combination of the properties of the constituent elements, their interactions, and the unique structure of the system that results in behavior that cannot be ascribed to any one component. The excess chemical potential, discussed in Section 2.2, for each component in the solution is thought to be the thermodynamic origin of these phenomena.[15] The term came about in Ranganathan's discussion of complex alloys[74] and was realized to be a core property of high entropy alloys.[37] The concept is apparent in HEOs as well, with evidence in catalytic applications being especially strong.[75] For example, Hao *et al.* created high entropy perovskite nanofibers for the purpose of alkaline oxygen evolution reaction. They found that their inclusion of Cu on the B-site out-performed perovskites of similar composition, as well as the commercially available standards.[76] Like with sluggish diffusion, this effect has been contested with regards to being a core property of high entropy materials. A difficulty with this effect is that it is not quantifiable and therefore difficult to prove. It has been suggested that this pertains specifically when there are 'exotic' properties that arise that cannot be predicted by a rule of mixtures,[54] as the enhancement of properties through synergistic interactions can be seen in materials without high entropy.[7,54,77]

2.4.5 Charge compensation

A particularly intriguing trait of HEOs is the charge compensation effect. In ceramics, the cations on a particular site ideally have a uniform valence directly balancing the anions to achieve

charge neutrality. However, when elements with differing electronic configurations are present, there are two possible mechanisms through which balance can be achieved. Firstly, a neighboring atom can undergo oxidation to account for the charge imbalance. For example, if Li^+ replaces Ni in a Ni^{2+} matrix, a neighboring Ni atom will oxidize and become Ni^{3+} in order to balance the charge of the local system.[78] Alternatively, charge compensation occurs through the formation of vacancies on the oxygen sublattice. Using the previous example of lithium in a nickel matrix, the introduction of an oxygen vacancy, $V_O^{\bullet\bullet}$, can offset two Li^+ substitutions.[78] The capability to substitute aliovalent atoms into a HEO lattice was first demonstrated by Bérardan *et al.* wherein elements of 1^+, 3^+, and 4^+ valence states were substituted into $(MgCoNiCuZn)_{0.2}O$.[56] This study showed that a single-phase rock salt structure was still formed with the addition of lithium up to equimolar proportions in a six-component material. Measuring the lattice parameter of this composition demonstrated compliance with Vegard's law, indicating Li was indeed substituted into the structure rather than occupying interstitial sites. The decrease in lattice parameter additionally suggests that charge compensation mechanisms occurred, either through oxidation of other cations or through formation of oxygen vacancies, as Li alone should increase the lattice parameter. Further, it was shown that the addition of 3^+ valence elements resulted in the formation of secondary phases whereas addition of equal proportions of 3^+ and 1^+ ions resulted in a single phase.

3. Local structure–property relationships

The compositional complexity and associated "disorder cocktail" in HEOs give rise to physical properties that can diverge from those of conventional oxides, depicted in Fig. 4. The influence of local structure on thermal, electronic, and magnetic behavior is particularly pronounced in HEOs due to their compositional complexity and structural flexibility. Table 1 provides a comparative summary of how various types of disorder impact these properties across representative systems. One hallmark is enhanced thermal and structural stability at elevated temperatures, a consequence of entropy-driven phase stabilization. Conversely, ESOs are prone to phase separation at lower annealing temperatures, where the entropic contribution to the free energy becomes insufficient to counter enthalpic driving forces.[151] These fundamental thermodynamic distinctions lay the groundwork for a wide spectrum of unique and tunable properties in HEOs. Thermal transport can be dramatically suppressed due to complex phonon scattering mechanisms, while ionic conductivity and catalytic activity are often enhanced by defect-rich, disordered environments. Magnetic behavior ranges from long-range order to spin-glass states depending on compositional tuning, and electrochemical stability can be achieved through selective redox participation of constituent ions. These examples underscore how configurational disorder not only modifies conventional property trends but also creates new opportunities for multifunctionality. The following highlights some of the examples of properties observed in various HEO compositions.

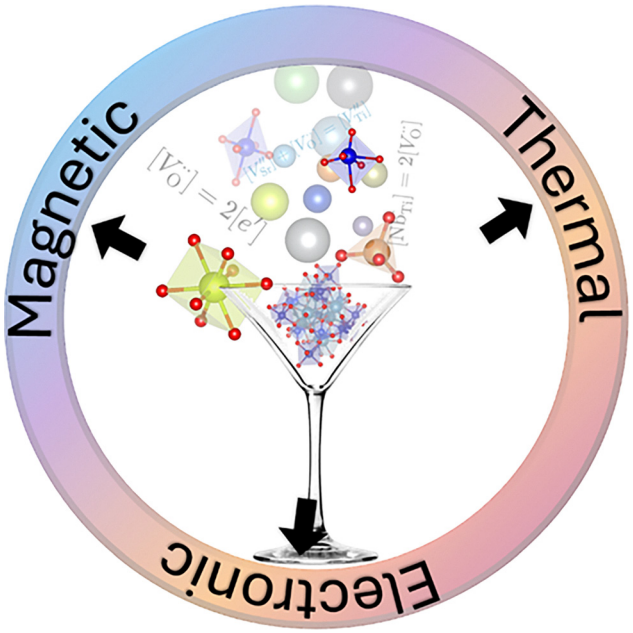

Fig. 4 The disorder cocktail in HEOs. Illustration depicting the types of local disorder including but not limited to point defects, cation charge and size variation, and polyhedral distortions, that may co-exist in any HEO system and the material properties they have been shown to impact.

3.1 Thermal conductivity

Thermal transport in HEOs is governed by complex phonon scattering mechanisms that go beyond conventional mass disorder. Recent studies have shown that charge disorder, lattice distortions, and compositional complexity can dramatically suppress thermal conductivity, offering new design strategies for thermoelectric and insulating materials.

Braun *et al.* investigated the thermal conductivity of $(MgCoNiCuZn)_{0.2}O$ and its six-component derivatives, finding that the observed ultralow values could not be explained by phonon scattering from mass disorder alone[84] Instead, their analysis pointed to Rayleigh-type scattering caused by large fluctuations in interatomic force constants originating from charge disorder, and subsequent localized polyhedral disorder, as a dominant mechanism. This deviation from conventional phonon scattering models also led to an atypical decoupling between thermal conductivity and stiffness: despite strong suppression of heat transport, the elastic moduli remained high, violating the typical correlation observed in non-metals.

Jana *et al.* extended this understanding to a novel high entropy niobate, $(SrBaLiKNa)_{0.2}Nb_2O_6$, which crystallized in a tungsten bronze structure and was designed for thermoelectric applications.[152] The measured lattice thermal conductivity approached the theoretical minimum ($\sim$0.7 W m^{-1} K^{-1}), with a value of 0.8 W m^{-1} K^{-1} at 470 K—indicative of glass-like thermal transport dominated by phonon scattering from point defects and structural disorder. Minimal electronic contribution

Table 1 Summary of average *versus* local structural features in key high entropy oxide (HEO) crystal systems and their implications for functional properties. While the average crystallographic structure determines long-range order, local chemical and structural disorder—driven by cation size/valence mismatch and oxygen sublattice distortions—plays a critical role in governing transport, ferroic, magnetic, and catalytic behavior. References are provided to guide further exploration of structure–property relationships across diverse HEO systems

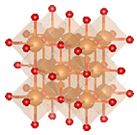	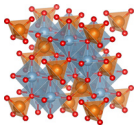	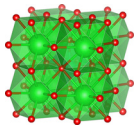	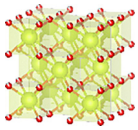	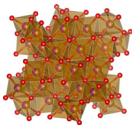	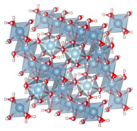	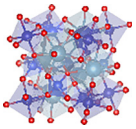	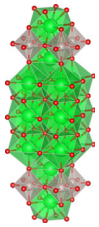
Rock salt ($Fm\bar{3}m$)	Spinel ($Fd\bar{3}m$)	Perovskite ($Pm\bar{3}m$)	Fluorite ($Fm\bar{3}m$)	Bixbyite ($Ia\bar{3}$)	Pyrochlore ($Fd\bar{3}m$)	Garnet ($Ia\bar{3}d$)	Ruddlesden–Popper ($I4/mmm$)
Cations occupy octahedral sites in a cubic lattice.	A-site (tetrahedral), B-site (octahedral); normal or inverse.	Ideal cubic or distorted ABO_3 lattice.	FCC with fully occupied cation lattice, disordered O sublattice.	Defective fluorite; two inequivalent cation sites, intrinsic O vacancies.	Ordered $A_2B_2O_7$ with corner-sharing BO_6 octahedra.	Complex framework of dodecahedral, octahedral, and tetrahedral sites.	Alternating perovskite and rock salt layers.
Strong local distortions due to size/valence mismatch; site-specific bond length variations.	Cation redistribution and SRO; B-site cation disorder common.	Octahedral tilting, local symmetry breaking; polar/non-polar domain coexistence in relaxors.	Strong local oxygen vacancy clustering, asymmetric cation-O environments.	Local distortions due to cation size/charge mismatch, vacancy clustering, potential site preference.	Local disorder on A and B sites; O′ disorder affects BO_6 connectivity.	Uneven local coordination geometries; site-specific bonding variations.	Interlayer strain, stacking faults, B-site order/disorder.
Affects thermal conductivity, electrical transport, and phonon scattering.	Alters redox activity, magnetism, and battery performance.	Enhances pyroelectric/ferroelectric response, local dipoles affect dielectric behavior.	Impacts oxygen ion mobility and redox cycling; critical for fuel cells and catalysis.	Influences optical transparency, ionic conductivity, and electronic structure.	Affects magnetic frustration, ionic conduction, and thermal robustness.	Critical for Li^+ transport in solid electrolytes; local distortions modulate conductivity.	Enables anisotropic ion/electron transport, relevant for thermochromics and cathodes.
56, 62 and 79–111	112–119	120–130	131–137	138–140	141–146	147	148–150

confirmed that heat conduction was governed primarily by lattice vibrations.

More recently, Riffe *et al.* demonstrated that broadband optical phonon scattering, intensified by compositional complexity and local lattice distortions, plays a central role in reducing thermal conductivity in multi-cation oxides.[153] Their combined experimental and computational study showed that diverse cation environments disrupt phonon lifetimes---particularly through optical modes providing a robust framework for tuning thermal transport beyond mass contrast effects alone.

3.2 Magnetism

There is a diverse range of magnetic behaviors that are highly sensitive to composition, structure, and site-specific interactions in HEO systems. $(MgCoNiCuZn)_{0.2}O$ demonstrates long-range antiferromagnetic ordering, despite containing only a subset of magnetic ions—Ni, Co, and Cu.[61,154] Reducing the concentration of these magnetic ions through chemical substitution alters the ground state, leading to spin-glass behavior, and subtle changes in composition have also been shown to influence the effective magnetic moment and the magnetic transition temperature.[154] In particular, J–T distortions modulated by the Cu content have been used to tune the degree of magnetic frustration and glassiness in the system.[60,155]

In perovskite-structured HEOs, magnetism is largely governed by B-site cations due to their direct role in mediating super exchange interactions.[60,156,157] However, A-site contributions become increasingly relevant at lower temperatures, where rare-earth elements can introduce localized magnetic interactions. Importantly, studies have revealed a clear relationship between the ionic radius of A-site cations and the Néel temperature, mediated through the Goldschmidt tolerance factor and its influence on the B–O–B bond angle.[156,157]

Krysko *et al.* examined the magnetic behavior of a single crystal high entropy aluminate spinel, $(MgMnFeCoNi)_{0.2}Al_2O_4$, and identified a cluster spin glass phase, evidenced by bifurcation in field-cooled, zero-field-cooled magnetization measurements.[158] This magnetic ground state reflects a combination of spin glass and antiferromagnetic behavior seen in the parent compounds, influenced by severe lattice distortion and magnetic frustration. Single crystalline high entropy spinel ferrites $(Mg_{0.2}Mn_{0.2}Fe_{0.2}Co_{0.2}Ni_{0.2})_x$-$Fe_{3-x}O_4$ were shown to exhibit sharp ferrimagnetic transitions up to 748 K, despite substantial cation disorder.[159] EXAFS analysis suggested a random cation distribution across lattice sites, which suppressed local clustering and short-range order up to $x = 1.8$, thereby enhancing magnetic homogeneity and preserving transition sharpness. These examples highlight how cation disorder and competing magnetic interactions in high entropy spinels give rise to complex magnetic ordering.

Overall, while the magnetic properties of HEOs often reflect those of their magnetic constituents, the ability to systematically vary composition enables precise tuning of magnetic ground states and transition temperatures. Such tuning offers a versatile platform for exploring frustration, glassiness, and emergent magnetic order.

3.3 Electronic properties

Several studies have explored the electrical properties of HEOs, revealing behaviors distinct from those of conventional ceramics. One early report identified a colossal dielectric constant ($>10^5$ at 373 K and 20 Hz) in $(MgCoNiCuZn)_{0.2}O$, suggesting significant potential for dielectric applications.[56] High entropy strategies applied to potassium sodium niobate (KNN) ceramics have yielded enhanced breakdown fields and high energy storage efficiency, attributed to grain refinement and the presence of polar nano regions.[160,161] Liu *et al.* observed high piezoelectric coefficients in high entropy perovskites, which correlated with increasing configurational entropy and were attributed to a flexible polarization configuration driven by lattice distortions.[233] Uniquely, the high entropy perovskites were shown to have a flexible polarization configuration stemming from lattice distortions. In addition to dielectric and ferroelectric properties, band gap tunability has been demonstrated in entropy-stabilized systems: Sarkar *et al.* used Pr substitution to modify the band gap in medium-entropy rare earth oxides,[234] while Chen *et al.* achieved both band gap tuning and improved breakdown strength in KNN-based HEOs through Hf and Ta doping.[161]

Uncovering the remarkable capabilities of HEOs holds great promise for the future of materials research. However, to fully exploit their tunability, it is essential to understand the underlying mechanisms by resolving the disorder and local structure features within these systems.

4. Characterization of local disorder in HEOs

Characterizing HEOs is both fundamentally necessary and greatly challenging. While macroscopic techniques such as XRD and SEM-EDS confirm the bulk symmetry and average elemental distribution of the system, they do not complete the picture. In HEOs, lattice distortions and defects often occur within the single-phase regime, and it is essential that materials be randomly homogenous at the atomic scale to maximize configurational entropy. Therefore, special emphasis must be placed on investigating the local structure, as it is this fine-scale arrangement that gives rise to many of the unique properties observed in HEOs. Given the distribution of cations across a single lattice site and the resulting angstrom-scale distortions, advanced techniques with high structural resolution and elemental selectivity are critical. This section highlights some of the premier characterization methods that fulfill these requirements, a more comprehensive list of techniques and associated references are in Table 2.

4.1 Spectroscopy

Spectroscopic techniques offer critical insight into the local structural, electronic, and magnetic environments of HEOs, complementing average structural data obtained by diffraction. These methods are particularly powerful in assessing cation valence states, site symmetries, bonding environments, and magnetic interactions—features often obscured in disordered, compositionally complex systems. Fig. 5 provides a comparative overview of the primary spectroscopic methods discussed in this section. We highlight the utility of X-ray magnetic circular dichroism (XMCD), Raman spectroscopy, electron energy loss spectroscopy (EELS), and Mössbauer spectroscopy in probing local structure and chemical behavior in HEOs.

4.1.1 X-Ray absorption fine structure. X-ray absorption fine structure (XAFS) is an extremely powerful technique for exploring the local structure of HEOs as it is sensitive to both the species and local environment of selected absorbers. XAFS is a spectroscopic technique that returns the absorption coefficient as a function of energy $\mu(E)$ through the Beer–Lambert law, $I_t = I_0 e^{-\mu x}$ or $\ln\left(\frac{I_0}{I_t}\right) = \mu(E)x$, where I_t and I_0 are the intensity of the transmitted and incident beams, respectively, and x is the sample thickness.

XAFS spectra is divided into two regions based on the source of the signal, XANES and EXAFS, which is delineated by the absorption edge. This spectral feature is the sharp increase in

Table 2 Summary of characterization techniques used to probe local and atomic-scale structure in materials science. Techniques are organized by the characteristic length scale probed, highlighting key features and types of structural or electronic information obtained. The rightmost column provides representative reference ranges for publications utilizing each method

Technique	Length scale	Key features	Information gained	Publications
X-ray absorption fine structure (XAFS)	2–6 Å	Element-specific, probes oxidation state and coordination	Coordination number, bond lengths, oxidation states	159 and 162–178
Pair distribution function (PDF)	~2–30 Å	Captures short- and medium-range order including amorphous phases	Atomic pair correlations in real space	179–185
Transmission electron microscopy (TEM)	0.1–10 Å	Atomic-resolution imaging; interface/defect analysis	Atomic positions, defects, grain boundaries	186–198
Electron energy loss spectroscopy (EELS)	~1–2 Å	Elemental & bonding information with atomic spatial resolution	Valence states, coordination, bonding	199–208
Atom probe tomography (APT)	Sub-nm (x, y); few nm (z)	3D atom-by-atom elemental mapping	Elemental identity and spatial distribution	209–213
Mössbauer spectroscopy	Atomic-scale	Sensitive to hyperfine interactions; element-specific	Magnetic/electronic environment at nuclei	214–222
Nuclear magnetic resonance (NMR)	Atomic-scale	Identifies local bonding & structure; useful in disordered systems	Chemical environments, short-range structure	223 and 224
Raman spectroscopy	Micron-scale (optical); vibrationally local	Non-destructive, bond- and phase-sensitive; suitable for mapping	Vibrational modes, bonding, symmetry, disorder, strain	225–232

the absorption coefficient associated with the energetic activation of the X-ray absorption mechanisms. The absorption edge is what allows this technique to be element specific as it loosely corresponds to the mass of the nucleus. The edge energy is sensitive to the charge state of the absorber, where the energy will increase as the ion's charge state increases. It has been shown that when compositions have the same species of ligand, this edge energy has a linear relation to the charge state.[235]

X-ray absorption near edge structure (XANES) is the region from around 100 eV before the edge to 30–50 eV above the absorption edge. The information in this region corresponds to the unoccupied states of the absorber. In addition to charge state, the XANES region can inform on the coordination environment through pre-edge peaks or shoulders in the spectra.[236]

Extended X-ray absorption fine structure (EXAFS) is from 30–50 eV after the absorption edge to continuum and this is the signal that results from the photoelectron scattering off the local environment and back to the absorber. The superposition of these interference waves is reported in reciprocal space by wavenumber ($Å^{-1}$) and is represented by the EXAFS equation,

$$\chi(k) = \sum_i \frac{N_i S_0^2}{kR_i^2} f_i(\pi,k) e^{(-2\sigma_i^2 k^2)} e^{\left(-\frac{2R_i}{\lambda_i(k)}\right)} \sin(2kR_i + \delta_c(k) + \delta_i(k))$$

. This data is not easily interpreted and is Fourier transformed into a partial-pair distribution function reported in real space (Å). The EXAFS region informs on the bond lengths, coordination, and geometry of the nearest and next-nearest neighbors of the absorber.

The analysis of XAFS data differs between the two regions. For EXAFS, data is modelled by an equation, which allows structural models to be fit by refining select parameters from the EXAFS equation—namely the path lengths, degeneracy of paths, and the Debye–Waller factor. The nuances of XANES data limit analysis to qualitative techniques. Fingerprinting is the most straightforward technique used where either calculated or measured standards are compared to experimental data to match spectral features corresponding to known differences.[237] The Demeter package of programs is the premier software for processing and analyzing XAFS data, with Athena used for processing and Artemis for EXAFS analysis.[238] These programs are coded in PERL and are unfortunately no longer supported, but Larch is written in Python and is actively being improved.[239]

XAFS has been leveraged to investigate the local structure of HEOs since their inception. Rost *et al.* used EXAFS to support the claim that the cations occupied the same site within rock salt in $(MgCoNiCuZn)_{0.2}O$ by comparing the partial pair distances for each absorber.[16] Subsequent studies have used XAFS to indicate charge compensation,[240] Jahn–Teller distortions,[59] and coordination.[241] XAFS measurements have been performed on $(MgMnCoNiFe)_xFe_{3-x}O_4$ single crystals to gain an understanding of trends seen in magnetization data, those being suppressed μ_B values from ferrimagnetic ordering and sharp magnetic transitions in a distorted structure.[242] XANES data reveals that both Fe and Mn exist in consistently mixed valence states throughout the series, with Fe showing a higher ratio of $3^+/2^+$ than pure Fe_3O_4 and Mn trending towards higher oxidation states as x increased. EXAFS data depicts a transition from

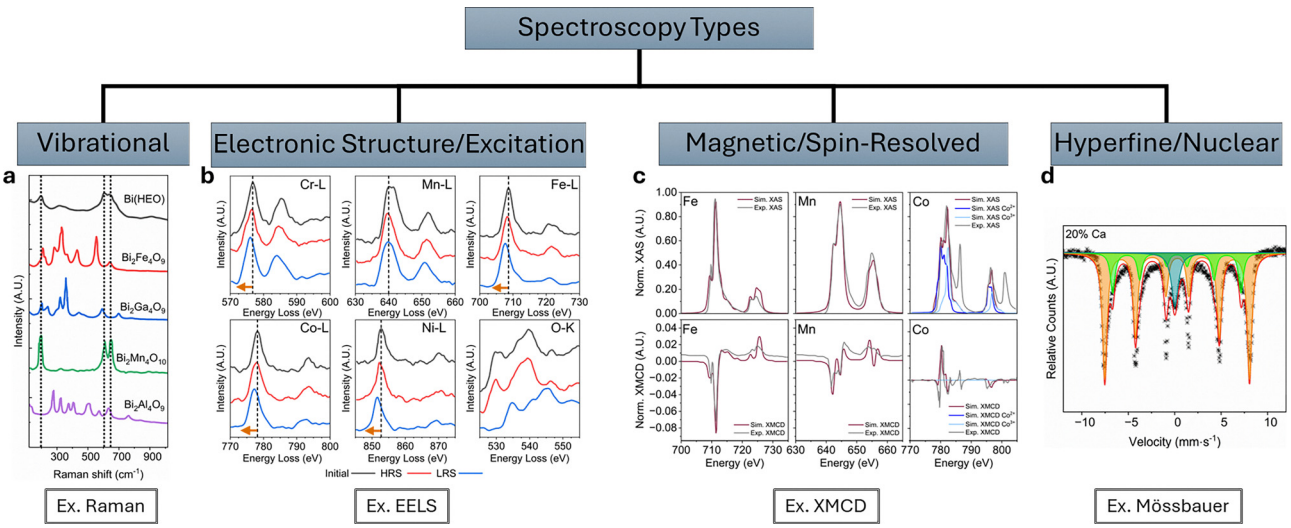

Fig. 5 Classification of spectroscopies typically used in the characterization on HEOs and example techniques representing them. (a) Raman spectra of $Bi_2(Al_{0.25}Ga_{0.25}Fe_{0.25}Mn_{0.25})_4O_9$ compared with parent compounds $Bi_2Al_4O_9$, $Bi_2Ga_4O_9$, $Bi_2Fe_4O_9$, and $Bi_2Mn_4O_{10}$. Spectral shifts and broadening indicate the effect of cation mixing on vibrational modes. Adapted under CC-BY-NC-ND 4.0 from Kirsch, *et al. Chem. Mater.* 2023 **35** (20), 8664–8674. (b) Electron energy loss spectroscopy (EELS) analysis of a Pt/$(CrMnFeCoNi)_3O_4$/Nb:STO resistive RAM device at different resistance states. Spectra for the L_2 and L_3 edges of Cr, Mn, Fe, Co, Ni, and the O K-edge show state-dependent changes in electronic structure. Black, green, and blue lines correspond to the initial, high-resistance, and low-resistance states, respectively. Reproduced with permission from J.-Y. Tsai *et al.*, *Adv. Mater.* 2023, **35**, 2302979. Copyright 2023, Wiley. (c) Fitted Mössbauer spectrum of 20% Ca in $(Gd_{0.2}La_{0.2}Nd_{0.2}Sm_{0.2}Y_{0.2})_{1-x}Ca_xFeO_3$ using two magnetic sextet models corresponding to Fe^{3+} and one singlet for Fe^{4+}. Reproduced through CC-BY-NC-ND from Eiselt *et al. Int J Appl Ceram Technol.* 2023; 20: 213–223 (d) X-ray absorption (XAS) and corresponding X-ray magnetic circular dichroism (XMCD) spectra for Fe, Mn, and Co (top and bottom panels, respectively), with experimental data and CTM4XAS fits recorded at 2.5 K. Adapted under CC BY from Regmi *et al. AIP Adv.* **14**, 025023 (2024).

a majority tetrahedral to octahedral occupation for the Mn cations as x increased as well.

4.1.2 X-ray magnetic circular dichroism. XMCD is a variant of X-ray absorption spectroscopy (XAS) that uses left- and right-circularly polarized light to probe the electronic and magnetic structure of materials.[243] The XMCD spectra is the difference of the left and right polarized scans. This technique retains the benefits of chemical and site sensitivity that is offered by XAFS through resonance energy and spectral features. Soft X-ray edges are advantageous to hard edges for XMCD as they drive dipole-allowed transitions to the magnetically active valence band. In a 3d transition metal, the core 2p state is split by spin–orbit interactions into spin 3/2 and 1/2 levels. The helicity of the incident light selectively excites electrons from one of these bands, corresponding to the L_2 and L_3 edges. The available holes in the 3d band dictate the sign of the signal that is output.[243] This translates accordingly to appropriate edges for elements with more complex electronic configurations. The dichroism can further inform on the site selectivity in materials. For example, the tetrahedral and octahedral sites in ferrite spinels have opposite magnetic alignments.[243] There are sum rules that allow the integral of the XMCD signal to be correlated to the orbital and spin magnetic moments.[244,245] This technique has been applied to HEO thin films to extract the magnetic orientation and interaction between elements within perovskite and spinel crystal systems.[246–248] Johnstone *et al.* conducted XMCD measurements on the L_3 edges of the transition metals in $(CrMnFeCoNi)_3O_4$ with varying amounts of Ga substitution to reveal charge and occupation trends for the individual cations.[249] Cr^{3+} and Ni^{2+} remain exclusively octahedral across the series; Fe^{3+} shifts from primarily tetrahedral to octahedral as Ga content increases; Co^{2+} transitions from fully tetrahedral to Jahn–Teller-distorted octahedral. Mn acts as the charge compensator, shifting toward Mn^{2+} as Ga content increases, accompanied by a transition from distorted octahedral to tetrahedral sites. In the 0% sample, Mn exhibits an average valence of $\sim 3.5^+$, decreasing to $\sim 2.5^+$ at 40% Ga. The XMCD-derived A- and B-site occupancies were used to estimate sublattice configurational entropy. While the total entropy exceeds the $1.5R$ high-entropy threshold, the octahedral site alone reaches this threshold with Ga substitution, and the tetrahedral site enters the medium-entropy regime ($>1R$), peaking at $x = 0.6$.

4.1.3 Raman spectroscopy. Raman spectroscopy allows examination of local structure by probing the vibrational modes of a material.[250] When monochromatic IR light interacts with a sample, it scatters and shifts in frequency depending on the vibrational modes of the material which are influenced by atomic arrangement, local bonding, and symmetry.[251] The frequency shift can be positive or negative, depending on whether the incident light gains or loses energy upon interaction with the sample. By analyzing these frequency shifts in terms of wavenumber (cm^{-1}), Raman spectra are obtained, with specific peaks corresponding to the different vibrational modes.[251] A positive shift in wavenumber, known as ''Stokes scattering,'' occurs when the material is excited to a higher vibrational state, reducing the energy of the scattered light. Conversely, a negative shift in wavenumber, called ''Anti-Stokes scattering,'' occurs when the material relaxes to a lower vibrational mode, increasing the energy of the scattered light.[250] If the scattered light retains the same wavelength as the incident light, it is known as Rayleigh scattering.[250]

In HEOs, the vibration of metal–oxygen bonds contributes to the distinct peaks in the Raman spectra.[252] Variation in species and bond lengths throughout the material causes dispersion of energies for vibrational modes, resulting in broadening and shifting of Raman peaks. The width and position of these altered peaks can be used to characterize the degree of disorder associated with specific bonds in the structure.[253] Raman spectroscopy has been used to help characterize the homogeneity in HEOs.[252] Raman spectroscopy has also been used to help determine the presence of oxygen vacancies in (CeLaPrSmY)O HEOs as a function of pressure.[254]

4.1.4 Electron energy loss spectroscopy. Electron energy loss spectroscopy (EELS) is commonly used in conjunction with electron microscopy to provide information about elemental composition, chemical bonding, and electronic structure of materials.[255] It is essentially the electron-based analog to XANES. This technique works by analyzing the energy loss of electrons as they pass through a sample, which gives insight into materials electronic structure and local environment.[255] EELS is typically performed in TEM or STEM setups, enabling it to be coupled with direct imaging techniques to gain complementary information about the sample. When the electron beam interacts with the sample, some electrons lose energy through inelastic scattering, leading to specific excitations within the material. These energy losses can be measured and used to extract valuable information regarding various material features, such as elemental composition, oxidation states, and bonding characteristics.[255,256]

EELS can be divided into two regions: low-loss and core-loss. These regions provide different types of information.[255] The low-loss region (typically from 0 to $\sim$100 eV) primarily provides information on the electronic structure of the material, such as the bandgap, plasmons, and inter-band transitions. This region can be useful for understanding the material's electronic properties but does not give direct elemental or chemical composition details. On the other hand, the core-loss region (typically above 100 eV) is focused on elemental and chemical analysis. In this region, electrons are excited from core-level orbitals to unoccupied states, which corresponds to characteristic absorption edges for different elements.[255] The K-edge and L-edge are often used to identify specific elements and their oxidation states. However, one limitation of EELS is its reduced sensitivity to lighter elements like oxygen, which makes analyzing these elements challenging.

EELS has been used by Ayyagari *et al.* to observe local variations in Mn and Co valency in a HEO thin film along its thickness.[257] Ayyagari also performed STEM-EELS in the Min *et al.* study to corroborate oxidation state findings from XANES measurements.[242] Phakatkar *et al.* employed EELS to determine the elemental homogeneity in a six-component HEO nanoparticle.[258]

Additionally, Kante *et al.* used EELS to analyze the oxidation states of constituent elements in HEOs, such as Cr, Mn, Fe, Co, and La, by examining the edge positions and intensity ratios of L_2/L_3 and M_4/M_5 edges, providing insights into charge transfer and the preferred valence states of transition metals and lanthanides.[259] EELS analysis of an HEO particle by Baek *et al.* showed varying oxidation states across its surface and bulk, with Fe^{2+} and Co^{3+} more prevalent on the surface, and Fe^{3+} and Co^{2+} toward the center.[260] The O K-edge data indicated higher oxidation states at the surface, likely due to mixed oxidation states across the particle.[260]

4.1.5 Mössbauer spectroscopy. The Mössbauer effect is the recoilless emission and resonant absorption of gamma rays (γ) by nuclei fixed in a solid.[261] When the γ source is oscillated to create a spectrum of photon energies, the resulting absorption data can provide information on the local electronic and magnetic environments of select atomic species. The γ source is an unstable isotope of $Z + 1$ to the targeted (Mössbauer active) isotope so that the when the source isotope decays, the emitted photons are resonant with the isotope in the sample and will thus be absorbed. In order for isotopes to be Mössbauer active, the γ energy needs to be sufficiently low for recoilless absorption and the lifetime of the excited state upon absorption needs to be relatively long to increase the resolution of the measurements.[262] There are several isotopes that are Mössbauer active, but ^{57}Fe is the most commonly probed due to its natural occurrence.[263] ^{57}Fe has γ energy of 14.4 keV and an excited state lifetime of 141 ns, correlating to a line width of 4.67×10^{-9} eV, which facilitates highly precise measurements.[262] The mechanism by which Mössbauer spectroscopy provides information is hyperfine interactions where the electron cloud surrounding the nucleus splits the nuclear levels. There are three major results of these hyperfine interactions that appear in the spectra and inform on the local environment of the target isotope.

Electric monopole interactions between protons and s-electrons that penetrate the nuclear field cause a shift in the observed spectra known as the isomer shift (δ). This shift is sensitive to the density and radial distribution of s-electrons, and it provides information on the valence state and chemical bonding of the isotope. Electric quadrupole interactions appear in the spectra as split resonance lines, with a spectral separation directly corresponding to the energy between nuclear substates. These interactions occur when nuclear states possessing a quadrupole moment are exposed to a non-zero electric field gradient. The electric field gradient arises from lattice asymmetry and anisotropic valence electron distributions, allowing the quadrupole splitting to inform on oxidation state, spin state, and local symmetry. In ^{57}Fe, this manifests in the spectra as a doublet. Magnetic dipole interactions occur when the nucleus possesses a magnetic moment and experiences a local magnetic field. The field lifts the degeneracy of the nuclear spin states and results in splitting into $2I + 1$ substates, where I is spin. The observed hyperfine splitting informs on the magnitude of the local magnetic field, which is caused by s-electron spin density at the nucleus, orbital motion of valence electrons, and/or total electron spin. This provides information about magnetic ordering and electron spin density in the material. In ^{57}Fe, these interactions manifest as a sextet of resonance lines, resulting from the excited state splitting into four sublevels and the ground state into two.[262]

This technique is extremely powerful for probing the electronic configuration and local magnetic environment of select isotopes with high precision. For HEOs containing Mössbauer active nuclei, it yields valuable insights on the local structure in such complex environments. It has been used to elucidate the site occupancy of Fe in spinels,[214,218–220] confirm magnetic ordering temperatures,[214,215,219] and determine oxidation state of Fe.[215,216,218] Eiselt *et al.* was able to discern magneto-electric phase separation in crystallographic single-phase high entropy perovskite through the presence of two different Fe^{3+} environments as well as Fe^{4+} compensating for vacancy formation, shown in Fig. 5(c).[215] Sarkar *et al.* discovered Néel-type collinear spin arrangement and site occupancy of Fe in an inverse high entropy spinel.[219]

4.2 Electron microscopy

Electron microscopy (EM), particularly scanning transmission electron microscopy (STEM), is a powerful imaging technique capable of resolving complex atomic structures and compositional variations in HEOs at sub-nanometer scales. Traditional methods like XRD provide average structural information but cannot reveal the subtle local ordering, nanoscale variations, or chemical segregations critical to the functional properties of HEOs. STEM bridges this gap with its atomic-scale resolution and energy-selective imaging capabilities.[264–266]

4.2.1 Scanning transmission electron microscopy. STEM employs a focused electron beam scanned across the sample, providing high spatial resolution. Its primary imaging modes—bright-field (BF), annular dark field (ADF), and high-angle annular dark field (HAADF)—offer distinct contrast mechanisms. HAADF-STEM, utilizing Rutherford scattering sensitive to atomic number (Z-contrast), effectively visualizes heavier metal cations but poses challenges for lighter elements like oxygen. Despite this limitation, HAADF-STEM has significantly contributed to understanding HEOs structures and morphologies. In Fig. 6(a)–(c), Su *et al.* revealed local ordering in high entropy perovskites using ABF to elucidate relationships between TM–O bond angles.[267] Huang *et al.* identified preferential ordering along specific crystallographic planes in $(CeYLaHfTiZr)_xO_\delta$ system.[268] Furthermore, Huang *et al.* used ADF to examine increased oxygen vacancies near HEO nanoparticle surfaces.[268] Almishal *et al.* utilized HAADF-STEM to directly observe nanoscale structural features in $(MgCoNiCuZn)_{0.2}O$ thin films, including cation-rich domains and the local emergence of distinct symmetry configurations.[40,269] Additionally, they demonstrate that HAADF-STEM can be used to generate strain maps, which are essential for understanding mechanisms of ordering evolution. These strain maps can then be integrated into developing complementary phase-field models, significantly enhancing predictive capabilities and accurately reproducing the experimentally observed nanoscale ordering. Fig. 6(d) shows an example of such HAADF-STEM strain maps for spinel-nano cuboids in the $(MgCoNiCuZn)_{0.2}O$

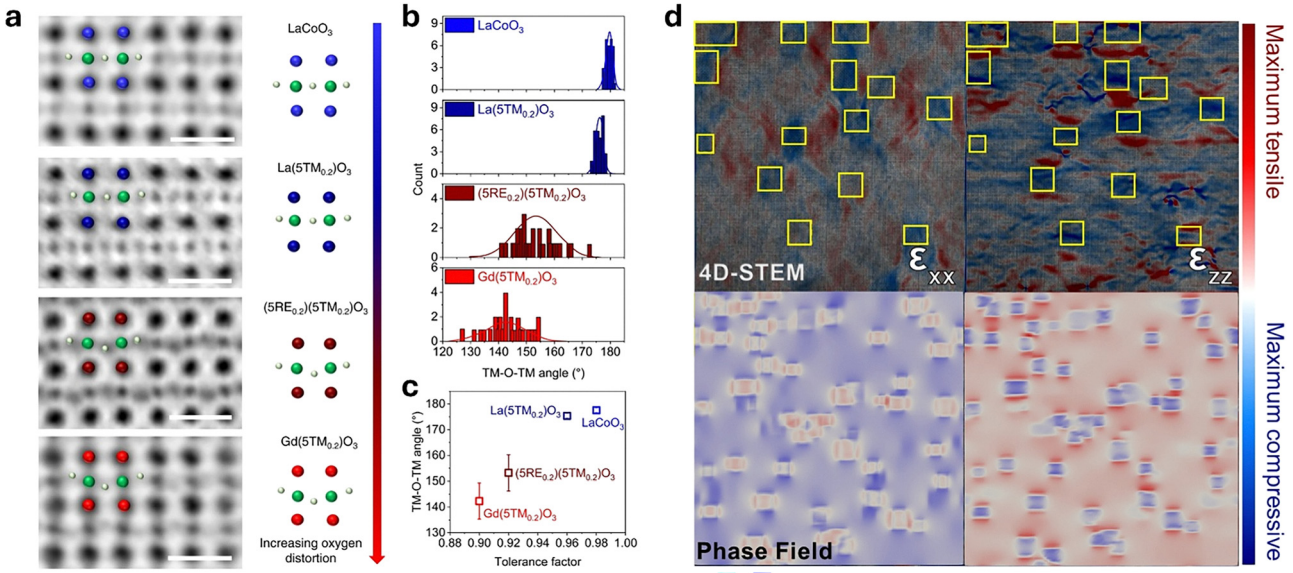

Fig. 6 (a) Annular bright field images of $LaCoO_3$, $La(CrMnFeCoNi)_{0.2}O_3$, $(LaNdSmGdY)_{0.2}(CrMnFeCoNi)_{0.2}O_3$, and $Gd(CrMnFeCoNi)_{0.2}O_3$, respectively, showing the transition metal–oxygen–transition metal (TM–O–TM) angle in their lattice structures. The green and silver spheres representing the B-site atoms and oxygen atoms, respectively, while the blue, dark blue, dark red and red spheres representing the A-site atoms in the four samples, respectively. Scale bar is 0.5 nm. (b) Distribution of the TM–O–TM angle in the four samples. (c) The relationship between TM–O–TM angle and tolerance factor. Data are presented as means of ± standard deviation of the distribution of TM–O–TM angle. (d) 4D-STEM mapping and phase-field modeling of nanoscale total elastic strain in a high-entropy $(MgCoNiCuZn)_{0.2}O$ matrix undergoing low-temperature order evolution at high thickness. The upper panels show in-plane (ε_{xx}, left) and out-of-plane (ε_{zz}, right) strain maps, where red and blue indicate maximum tensile and compressive fields, respectively, as measured by 4D-STEM. Yellow boxes highlight spinel nanocuboids with localized elastic heterogeneities. The lower panels present phase-field reconstructions revealing the spatial distribution of order, distinguishing lower-entropy offspring structures that emerge through the interplay of thermal history and elastic–chemical boundary effects. Figures a through c were reproduced though a CC-BY license from Su, *et al. Nat. Commun.* **13**, 2358 (2022). Figure d was adapted though a CC-BY from Almishal, *et al. J. Am. Ceram. Soc.* **108**, e20223 (2025).

thin films and the corresponding simulated strain maps from phase field modeling. Several studies have employed HAADF-STEM in combination with EELS to investigate elemental distribution and oxidation states in HEOs. For example, the aforementioned spinel nano cuboids were found to exhibit elevated concentrations of Co^{3+},[40] while in $CuCeO_x$–HEO nanoparticle systems, CeO_2 particles were observed to graft onto the surface of HEO particles.[270] These techniques have also been used to probe strain and cation distribution at grain boundaries, often associated with oxygen deficiencies.[271]

Jiang *et al.* used ADF-STEM with EDS to examine nanoscale homogeneity of B-site cations in high entropy pyrochlore compositions and confirm composition stoichiometry for data models.[272] Zhang *et al.* used SEM-EDS, HAADF-TEM with EDS, and HRTEM to investigate the structure of $(CaSrBaLaPb)_{0.2}TiO_3$ to discover the impact of local disorder on transport properties.[273] SEM and HAADF-TEM imaging confirmed that there was homogenous A-site cation distribution after sintering and post-annealing. HRTEM revealed 4–6 nm grains with irregular orientations and edge dislocations, particularly at grain boundaries, that introduced strain fields. These strain fields coupled with structural distortions and cation disorder disrupted phonon transport, producing a lattice thermal conductivity of 1.75 W m^{-1} K^{-1} at 1073 K.

Emerging STEM-based techniques like integrated differential phase contrast (iDPC-STEM), annular bright-field (ABF-STEM), and four-dimensional STEM (4D-STEM) offer complementary analytical strengths. ABF-STEM significantly improves oxygen detection and facilitates detailed oxygen vacancy mapping. Additionally, machine learning methods have become crucial for analyzing extensive and complex TEM datasets, providing rapid and quantitative identification of subtle structural and chemical ordering. Therefore, the integration of electron microscopy, advanced analytical techniques, computational modeling, and machine learning establishes a comprehensive framework for resolving the intricate structural and chemical complexities inherent in HEOs at the local scale. Such multi-scale, multi-modal approaches are essential for engineering next-generation oxide materials with tailored functionalities.

4.2.2 Atom probe tomography. APT is a hybrid microscopy technique that provides a compositional map with three-dimensional spatial resolution and chemical sensitivity. Samples are fabricated in a needle-like structure with an apex tip radius typically <100 nm and held at cryogenic temperatures in an ultra-high vacuum chamber to minimize unprompted evaporation and ionization. Measurements are facilitated by high-voltage pulses in conjunction with femtosecond laser pulses to systematically evaporate ions from the sample. Once evaporated, ions travel up to 200 mm to a position-sensitive detector comprised of microchannel plates to elucidate initial position and time-of-flight (TOF). The TOF data is correlated to the mass-to-charge ratio of ions to resolve the chemical species of each impact through the relation $m/n = 2eVt^2/L^2$, which allows for this to be applied to the full range of the periodic table. The detector

records the (x,y) position of the impacts and reverse projects the positions to a dynamically updated quasi-stereographic projection model to determine the z-position of the ions. This technique provides truly atomic-scale precision as the spatial resolution is 0.2–0.3 nm laterally and 0.1–0.2 nm in depth.[274]

Studies have demonstrated the power of APT in elucidating nanoscale chemical fluctuations and phase formation mechanisms in HEO systems. Correlative APT and TEM to reveal that controlled cooling of $(MgCoNiCuZn)_{0.2}O$ leads to partial phase separation and local clustering, particularly of Cu, even when XRD indicates a nominally single-phase structure.[213] These subtle chemical redistributions underscore the need for atomic-scale compositional analysis in interpreting stability and functional behavior. Building on these insights, Dupuy *et al.* combined APT and TEM to examine the nucleation and growth of secondary phases in $(MgCoNiCuZn)_{0.2}O$.[211] They observed that Cu-rich and Co-rich regions, initially maintaining rocksalt-like structure, served as precursors to the formation of crystalline tenorite and spinel, respectively. These transformations were spatially localized and facilitated by cation vacancies and local structural distortion. Importantly, elemental segregation preceded crystallization, supporting a non-classical nucleation pathway, and growth was governed by cation diffusion through the parent matrix. Gwalani *et al.* applied APT to a Y_2O_3-doped high-entropy alloy and discovered the *in situ* formation of compositionally complex nanoscale oxide dispersoids.[187] The oxides exhibited high configurational complexity with contributions from multiple cation species, supporting the notion of entropy-stabilized secondary phases. Collectively, these results reinforce APT's unique ability to detect early-stage, nanoscale inhomogeneities that influence macroscopic behavior in HEOs.

4.3 Total scattering

Total scattering is a technique that collects the entire scattering signal from a material to resolve the structure on multiple length scales. The intricacies of total scattering are outside the scope of this review, but in-depth discussion of them can be found in books and reviews.[275,276] To be brief, the scattering vector, Q, is combined with atomic specific variables to create the scattering function $S(Q)$. It can be seen in $Q = 4\pi \sin(\theta)/\lambda$ how sharp peaks will appear when the Bragg condition for constructive interference, $1/d = 2\sin(\theta)/n\lambda$, is fulfilled.[277] The periodic lattice positions are captured in this Bragg diffraction to give the long-range order of the system. The deviations from the perfect lattice though local disorder, defects, and short-range order are communicated in the diffuse scattering. $S(Q)$ captures both signals in reciprocal space and is Fourier Transformed to create the pair distribution function (PDF) of interatomic distances in real space. Being a Fourier Transform, the maximum resolution of the PDF will be achieved by maximizing the range of Q that is probed.

4.3.1 X-ray scattering. Using X-rays as the scattering radiation to collect PDF (xPDF) data means that the atomic form factor must be taken into account. X-Rays interact with the electronic orbitals around nuclei and the atomic form factor is a function of the electron density as well as Q, meaning it will scale with Z and change with the scattering angle. This form factor limits the momentum transfer space available in xPDF due to the fact that the intensity of scattering decreases as angle increases.[277] The high flux of photons from synchrotron sources can make measurement feasible at higher angles and have the benefit of shorter collection times.[275,277] Laboratory xPDF instruments are also available that utilize sources with shorter wavelengths, such as Mo or Ag, to increase the Q range.[275]

4.3.2 Neutron scattering. Neutrons scatter off of the nuclei of atoms, giving neutron PDF (nPDF) measurements the leg up on xPDF in a couple of aspects. The smaller size of the nuclei compared to the electron orbitals renders the atomic form factor to 1 for all Q, maximizing the momentum transfer space that is visible.[277] Nuclei also have characteristic cross-sections and scattering lengths that allow for sensitivity to light elements, down to H.[278] Neutrons have spin 1/2, giving them a magnetic moment and allowing them to probe the magnetic structure of materials based on the magnetic interaction operator and the magnetic form factor.[279] These aspects are especially important for HEOs where there is a mixing of cations with varying levels of magnetism, the common inclusion of Mg or Li, and dislocations under an angstrom.

Min *et al.* performed neutron diffraction on high entropy ferrite spinel single crystals to confirm sharp magnetic transition temperatures and support the assumption of ferrimagnetic ordering.[242] Jiang *et al.* utilized neutron diffraction to characterize average structure in high-entropy pyrochlores $Nd_2(Ta_{0.2}Sc_{0.2}Sn_{0.2}Hf_{0.2}Zr_{0.2})_2O_7$ and $Nd_2(Ti_{0.2}Nb_{0.2}Sn_{0.2}Hf_{0.2}Zr_{0.2})_2O_{7+x}$.[272] The diffractogram matched with cubic $Fd\bar{3}m$, although Rietveld refinement revealed that orthorhombic *Imma* resulted in a stronger fit. Analysis of the anisotropic atomic displacement parameters (ADPs) revealed that the oxygen anisotropic displacement ellipsoids of the TiNb compound are prolate rather than the spherical ellipsoids of the TaSc compound, indicating higher distortion of the MO_6 octahedra. Johnstone *et al.* conducted powder neutron diffraction measurements on $(CrMnFeCoNi)_3O_4$ with varying amounts of Ga doping to elucidate the magnetic structure of the material.[249] The diffractograms revealed that there was a propagation vector of $k = 0$, allowing for the determination that both sites occupy the Γ9 state. This indicates that the tetrahedral and octahedral sites are ferromagnetically oriented in the ⟨100⟩ direction and antiparallel to one another, supporting magnetization measurements.

4.3.3 PDF analysis. The local disorder characteristic to HEOs makes total scattering a powerful technique for elucidating the structure of the system. Least-squares refinement of the real space data can be used to fit structural parameters of a model, including the unit cell, atomic displacements, and occupations. PDFfit2 is an application to do this built on Python and has the user friendly PDFgui built upon it that includes macros for temperature, doping, and r series fitting.[280] Another analysis technique is using Reverse Monte Carlo simulations to refine structural models based on the total scattering data. An example of such simulations combined with neutron experimental data,

$G(r)$, and partial pair correlations is shown in Fig. 7. RMCProfile is a program that can do this for a supercell, building the model using individual atomic moves and outputting the structure along with information such as atomic displacements, and has recently been updated to allow the simultaneous consideration of both total scattering and EXAFS data.[281] The power of total scattering to discover differences in the local structure of HEOs from the average structure has been utilized in numerous studies to date.[61,282]

Jiang *et al.* used both PDFgui and RMCProfile to perform small and large box modeling of nPDF data collected on high entropy pyrochlores.[272] The r series fitting was utilized in PDFgui to fit 1.5–10 Å and 10–30 Å independently. The medium range was well fit by both the *Imma* and $Fd\bar{3}m$-ADP models for both compositions. The local structure range for the TaSc sample was also well fit by both models, but the TiNb fit was appreciably better with *Imma*. This is evidence that there are differing local distortions between the compositions. Additionally, below 2.6 Å in the TiNb data was not matched by any space groups. Fig. 7 depicts the results of the RMCProfile fitting out to 6 Å as well as the partial pair correlations for the M–O pairs, including analysis of peaks associated with the first M–O shell. The refined supercell resultant from this fitting confirms the trends that were predicted by AIMD simulations, namely the shorter Ta–O bonds and J–T distortions in the TiO_6 octahedra. Folding the supercell into a single $Fd\bar{3}m$ unit cell confirms ADP trends that were observed in Rietveld fitting of the neutron diffractograms, indicating larger degrees of distortion in the TiNb sample. Statistical analysis of cation pairs across 10 models generated by RMC were used to roughly calculate Warren–Cowley SRO parameters. These calculations revealed a negative value for Ti–Ti pairs, indicating a level clustering.

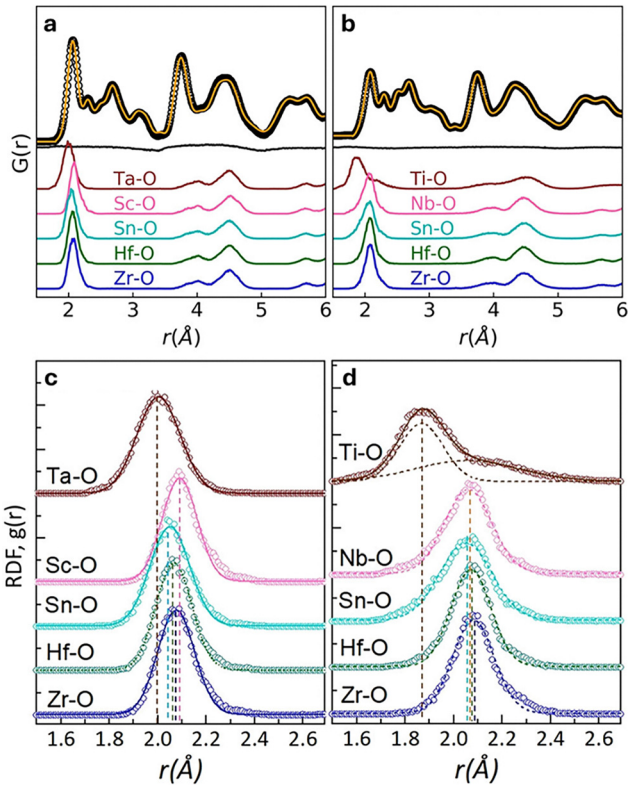

Fig. 7 Experimental $G(r)$ (black circles) and Reverse Monte Carlo simulation (orange lines) for (a) $Nd_2M_2O_7$ with M = Ta, Sc, Sn, Hf, Zr, and (b) $Nd_2M_2O_7$ with M = Ti, Nb, Sn, Hf, Zr, with partial pair correlation functions from models shown below as separate, labeled, colored lines. Gaussian peak fitting of the first M–O pair–pair correlation peaks from the RMC partial PDF distributions in (c) $Nd_2M_2O_7$ with M = Ta, Sc, Sn, Hf, Zr, and (d) $Nd_2M_2O_7$ with M = Ti, Nb, Sn, Hf, Zr. A double deconvoluted Gaussian peak was used to fit the Ti–O bond distribution peaks. Reprinted with permission from Jiang *et al. J. Am. Chem. Soc.* 2021, **143**, 11, 4193–4204. Copyright 2021, ACS.

4.4 Computational methods

Computational methods are essential in helping understand the local structure of novel materials through system modeling. There are a variety of approaches to predict the local structure of a material using principles of quantum mechanics and statistical mechanics to model atomic interactions. Methods such as molecular dynamics, density functional theory, and Monte Carlo simulations have been used to study high entropy materials.

Molecular dynamics (MD) is a computational model that solves Newton's equations of motion to equilibrate the system based on approximate effective potentials.[283] This method has been used to model edge dislocation density in HEOs[284] and study oxygen self-diffusion in a fluorite-structured HEO.[285] This method has also been used to predict properties of a high entropy carbide with good correlation to experimental results.[286] Due to the complexity of interactions present in high entropy materials, *ab initio* molecular dynamics (AIMD) may be an advantageous route to follow. Where MD uses Newton's equations, AIMD uses the Schrodinger equation to allow for real potentials to model quantum effects.[283] AIMD has been used to model thermal fluctuations that inform density functional theory calculations to simulate local environments in HEOs.[272]

Density functional theory (DFT) is a method of computing the electronic structure of materials using electron density rather than wave function theory, which reduces the computational cost of modeling systems.[287] DFT can be used to predict thermodynamic stabilities, electronic structures, and defect formation energies with good accuracy.[288] Due to the large configurational space of HEOs it is difficult to test an entire range of material compositions, but DFT can help screen desirable candidates.[289] DFT has been used in this manner to help investigate a novel catalyst composition for an oxygen evolution reaction.[290] Vienna *ab initio* simulation package (VASP) is a DFT software which uses plane-wave approximations and is commonly applied to HEOs.[291–293]

Monte Carlo simulations are a statistical technique used to predict outcomes by modeling random processes and estimating probabilities based on input parameters.[294] This method generates a range of possible results by varying input factors, such as atomic configurations, energy states, or temperatures, according to predefined probability distributions.[294] These simulations are useful for modeling HEO systems, where factors like disorder and multi-component mixing play crucial roles. Monte Carlo methods have been applied to predict

material behaviors such as magnetic response[295] and component segregation as a function of temperature.[293] A Monte Carlo model developed for HEO perovskites by Motseyko *et al.* showed that the order–disorder transition temperature (T_{od}) correlates with the standard deviation of cation–anion bond lengths, offering a simple way to estimate T_{od} in multi-cationic materials like HEOs.[296]

5. HEO characterization toolkit

Obviously, all the techniques described in this review are regularly used on a variety of materials spanning all levels of compositional and structural complexity. To that point, when investigating the novel phenomena that occur in HEOs, the observed property changes often admit competing explanations. With the disorder in these materials spanning a broad spectrum of modes, similar (and dissimilar) elemental species, and length scales in a single phase, one single measurement type can often miss or misattribute the origin of a feature. Only when corroborating multiple data sets do the pieces of the puzzle fit together. Understanding the local structure in HEOs requires careful consideration of the limitations inherent to individual characterization techniques, particularly with respect to the length scales they probe. For instance, XRD is a powerful tool for identifying average crystal structures and long-range order, but it often fails to detect nanoscale disorder, short-range chemical correlations, or subtle symmetry distortions that may be central to the material's functional behavior. Because XRD is primarily sensitive to periodicity, it can obscure meaningful local deviations that exist within an overall crystalline matrix. Other techniques, such as SEM or EDS, provide valuable morphological and compositional information, but may lack the spatial or chemical resolution needed to distinguish homogeneous solid solutions from locally segregated environments. As a result, conclusions drawn from a single technique risk oversimplifying the material's complexity. A comprehensive understanding of local structure in HEOs therefore necessitates the integration of multiple complementary methods, such as PDF analysis, XAS, and HRTEM, to bridge the gap between local and average structure and provide a more complete picture. When working on something as simplistic as a bicycle, there is the need for a variety of common tools to accomplish a project such as allen and cresent wrenches. Even still, there are specialty tools that are needed such as spoke wrenches and chain separators. This analogy raises the point that it is necessary to be mindful of the task needing completion (phase and structure characterization) as well as the object (a highly complex material system) that is having work done to it.

An excellent compilation of work by Sarkar *et al.* demonstrates the complexity of experimentally characterizing an HEO system at all length scales to enable a full-scale picture of the material and its subsequent properties.[219] Fig. 8 depicts several key characterization techniques used in their experimental strategy that are reviewed in this article, starting with confirming the phase purity of the sample and bulk magnetic behavior before stepping down to the specific magnetic structure and local environments. Such work illustrates the necessity of the combined and cross-correlated experimental techniques, and while many experiments may require varying characterization methods depending on specific goals of the work (*e.g.* Sarkar, *et al.* did not need EXAFS) and compositions (Mössbauer is only valuable for Fe-containing systems), the message is that there is no simple way to gain a realistic picture of HEO systems.

6. Summary and prospect

Local structure plays a defining role in determining the functional properties of HEOs, and continued progress in the field will rely on a deeper, more quantitative understanding of how chemical disorder manifests at the atomic scale. While a wider range of tools including XAFS, STEM/EELS, total scattering, and Raman spectroscopy among others, have proven invaluable, the true opportunity lies in integrating these techniques into unified, multi-scale characterization frameworks. The integration is essential to link subtle variations in local coordination, bond length distributions, and valence fluctuations to emergent properties such as ionic transport, magnetism, and electronic response.

A major future direction involves decoupling the contributions of disorder of different sublattices. In complex oxide systems such as spinels, perovskites, and pyrochlores, the A and B sites often host cations with different valences, ionic radii, and bonding preferences. As demonstrated in the spinel and perovskite HEOs,[249,273,297] the ability to selectively control disorder on one sublattice while maintaining order on another provides a unique mechanism to tailor properties. Future studies should explore the entropy balance between sublattices, using a combination of synchrotron-based EXAFS,[59,149,298] neutron scattering,[299,300] and configurational entropy calculations derived from site occupancy analysis *via* STEM-EDS/EELS.[249,257,258,301] Site-specific entropy tuning wherein only one sublattice meets the 1.5R threshold may enable property optimization without compromising structural coherence.

Another promising area lies in advancing total scattering and PDF techniques. The capacity of total scattering to resolve structural information across both short- and intermediate-range order is particularly valuable in HEOs, where distortions often occur without changing average symmetry. PDF analyses, when performed using boxcar or variable-r fitting schemes, can reveal how the local environment evolves as a function of composition, thermal history, or external field. Coupling these with RMC simulations allows for atomistic reconstructions that reflect real-space disorder.[299] The simultaneous refinement of EXAFS and PDF data within the same structural model, now feasible using tools such as RMCProfile,[281,302] represents a critical next step. Such joint modeling can enhance confidence in assigning coordination environments and quantifying bond length distributions.

In parallel, the role of the oxygen sublattice remains comparatively underexplored. Given the prevalence of charge compensation *via* oxygen vacancy formation in aliovalent-doped

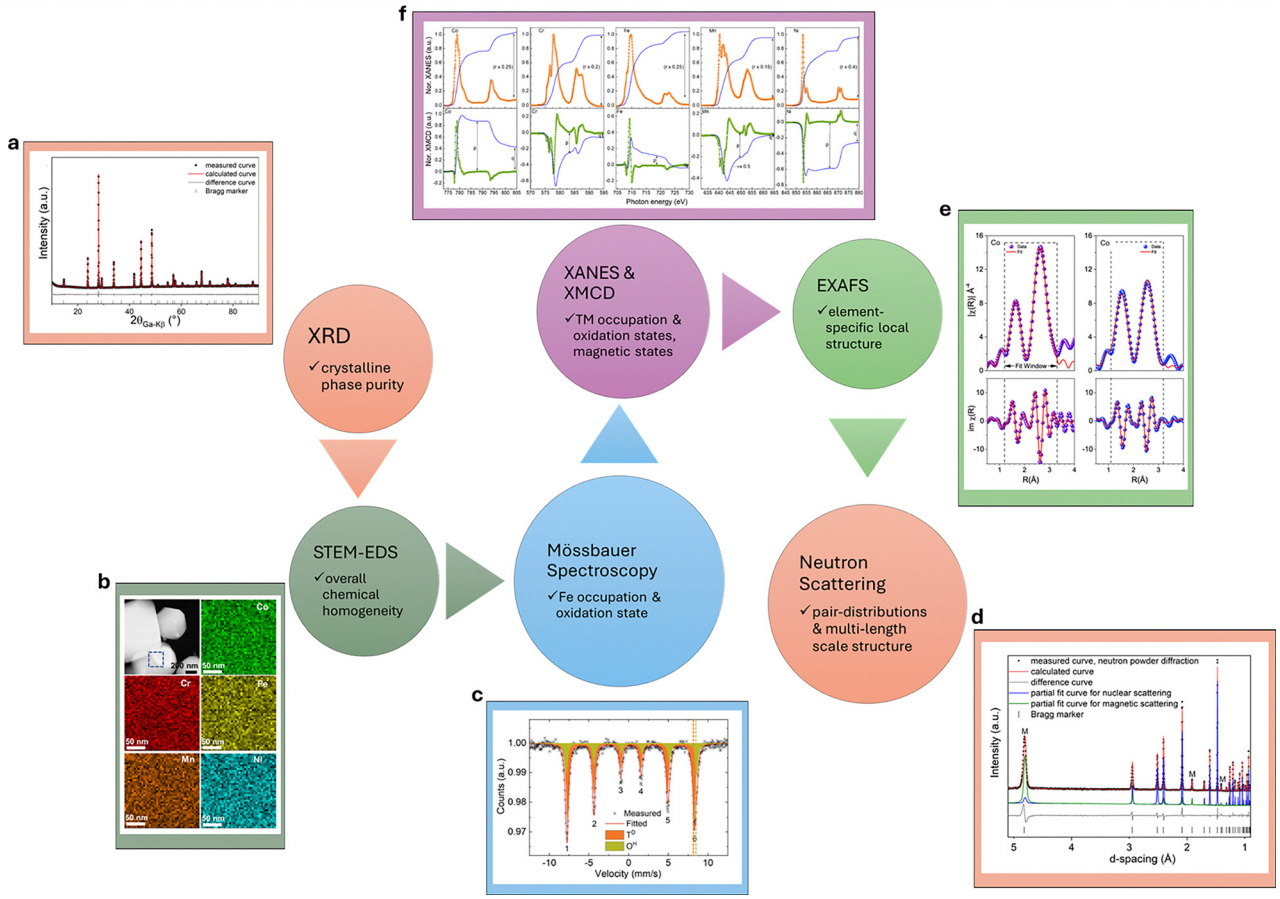

Fig. 8 A schematic representation of an ''HEO Characterization Toolkit'', the experimental characterization typically needed to complete a comprehensive picture of the high entropy oxide structure including but not limited to (a) X-ray diffraction, (b) STEM-EDS, (c) Mössbauer spectroscopy for Fe-containing systems, (d) neutron scattering, (e) EXAFS, and (f) XANES and/or XMCD (if containing magnetic elements). This representation is largely based on the work by Sarkar, *et al.* in understanding the enthalpy/entropy balance as well as crystal and magnetic structure in transmission metal (TM) spinel-based HEO $(Co_{0.2}Cr_{0.2}Fe_{0.2}Mn_{0.2}Ni_{0.2})_3O_4$. Such work illustrates the necessity of the combined and cross-correlated experimental techniques, and while many experiments may require varying characterization methods depending on elemental composition, the take-away is that there is no simple way to gain a realistic picture of HEO systems. All figures but EXAFS reproduced from Sarkar *et al. Acta Materialia*, 226, 2022, 117581 with permission from Elsevier. EXAFS reproduced from Braun, *et al. Adv. Mater.* 2018, **30**, 1805004.

HEOs,[303,304] future work should incorporate O K-edge XAS, neutron total scattering and Raman spectroscopy to systematically map oxygen coordination and vacancy clustering. These effects not only impact ionic conductivity and redox behavior,[75] but may also influence magnetic ordering and dielectric response *via* lattice distortions. Advanced techniques such as aberration-corrected STEM coupled with 4D-STEM and ABF imaging may offer additional sensitivity to light elements like oxygen,[268] helping to map subtle off-stoichiometry and detect soft-mode distortions.

A further direction involves the development of *in situ* and *operando* techniques to capture dynamic structural evolution under functional conditions. While most studies of local disorder rely on static measurements, real-world applications often involve high temperatures, electric fields, or reactive environments. The use of *in situ* XANES, Raman, or diffraction under applied stimuli (*e.g.*, electric field, temperature, partial pressure) could uncover how local environments reconfigure during device operation or catalysis.[76] For example, tracking cation oxidation states and coordination environments during electrochemical cycling could clarify charge/discharge mechanisms and structural degradation pathways in energy storage applications.[100,305]

Advances in data science and machine learning (ML) offer transformative potential for accelerating the characterization of HEOs. As the number of compositional permutations and structural configurations in HEOs grows exponentially, ML techniques can help uncover correlations between atomic-scale disorder and macroscopic properties. Recent studies have applied unsupervised clustering of XANES spectra, automated segmentation of STEM images, and high-throughput DFT screening to inform compositional design and phase stability trends.[234] However, integrating data across techniques remains a challenge, as each method is grounded in distinct physical principles and mathematical frameworks. Future progress will require the development of unified ML/AI platforms capable of simultaneously analyzing spectroscopy, diffraction, and microscopy data to quantify local disorder and predict functional performance. Such tools would not only accelerate interpretation but could also guide

experimental design by identifying promising compositional regions with targeted specifically by disorder characteristics. A platform that seamlessly connects multi-modal datasets to structural models and property predictions would represent a major milestone in the field, one that could shift the paradigm from characterization to true materials-by-design.

Against this backdrop, it can be surmised that HEOs represent a rapidly growing frontier in materials science, where chemical disorder and configurational complexity give rise to remarkable functional behavior. Over the past decade, significant advances have been made in understanding how structural disorder, charge compensation, and lattice distortions contribute to the macroscopic properties of HEOs. However, much of this insight has focused on average structure or compositional trends. As this review has shown, the local structure encompassing short-range order, site-specific coordination, and nanoscale symmetry breaking is increasingly recognized as the true origin of many functional phenomena in HEOs.

In this context, the next generation of HEO research will hinge on our ability to bridge local structural motifs with property outcomes across thermal, electrical, magnetic, catalytic, and electrochemical domains. This effort will demand more than the individual application of advanced characterization tools; it will require synergistic integration of experimental, computational, and data-driven methodologies. Multi-modal investigations combining, for example, X-ray absorption spectroscopy, total scattering, STEM-EELS mapping, and DFT-based modeling, can offer a more complete picture of disorder, but only when interpreted through a unified framework.

Harnessing this potential will require a new level of collaboration across synthesis, theory, and characterization. As our understanding of disorder deepens, so too will our ability to exert predictive control over functionality, ushering in a new era of materials-by-design built not around idealized order, but around the creative engineering of disorder itself.

Author contributions

John P. Barber: conceptualization, data curation, writing – original draft, writing – review & editing, supervision. William J. Deary: data curation, writing – original draft. Andrew N. Titus: data curation, writing – original draft. Gerald R. Bejger: data curation, writing – original draft, writing – review. Saeed A. I. Almishal: data curation, writing – original draft, writing – review & editing. Christina M. Rost: conceptualization, data curation, visualization, writing – original draft, writing – review & editing, funding acquisition, supervision.

Conflicts of interest

The authors have no conflicts to declare.

Data availability

No primary research results, software or code have been included, and no new data were generated or analyzed as part of this review.

Acknowledgements

The authors gratefully acknowledge support through NSF MRSEC DMR-2011839. C. M. R. also acknowledges partial support from NSF through the Faculty Early Career Development Program (CAREER), DMR-2440979.

References

1 C. Marcos, *Crystallography: Introduction to the Study of Minerals*, Springer Nature, Switzerland, Cham, 2022.
2 J. R. Woodyard, *US Pat.*, US2530110A, 1950.
3 F. Seitz, *Phys. Today*, 1995, **48**, 22–27.
4 G. N. Kotsonis, S. S. I. Almishal, F. Marques dos Santos Vieira, V. H. Crespi, I. Dabo, C. M. Rost and J.-P. Maria, *J. Am. Ceram. Soc.*, 2023, **106**, 5587–5611.
5 C. Oses, C. Toher and S. Curtarolo, *Nat. Rev. Mater.*, 2020, **5**, 295–309.
6 H. Xiang, Y. Xing, F. Dai, H. Wang, L. Su, L. Miao, G. Zhang, Y. Wang, X. Qi, L. Yao, H. Wang, B. Zhao, J. Li and Y. Zhou, *J. Adv. Ceram.*, 2021, **10**, 385–441.
7 D. B. Miracle and O. N. Senkov, *Acta Mater.*, 2017, **122**, 448–511.
8 B. L. Musicó, D. Gilbert, T. Z. Ward, K. Page, E. George, J. Yan, D. Mandrus and V. Keppens, *APL Mater.*, 2020, **8**, 040912.
9 M. Brahlek, M. Gazda, V. Keppens, A. R. Mazza, S. J. McCormack, A. Mielewczyk-Gryń, B. Musico, K. Page, C. M. Rost, S. B. Sinnott, C. Toher, T. Z. Ward and A. Yamamoto, *APL Mater.*, 2022, **10**, 110902.
10 C. M. Rost, A. R. Mazza, S. J. McCormack, K. Page, A. Sarkar and T. Z. Ward, *Appl. Phys. Lett.*, 2024, **125**, 200401.
11 S. V. Krivovichev, V. G. Krivovichev, R. M. Hazen, S. M. Aksenov, M. S. Avdontceva, A. M. Banaru, L. A. Gorelova, R. M. Ismagilova, I. V. Kornyakov, I. V. Kuporev, S. M. Morrison, T. L. Panikorovskii and G. L. Starova, *MinMag*, 2022, **86**, 183–204.
12 T. A. Olds, J. Plášil, A. R. Kampf, A. Simonetti, L. R. Sadergaski, Y.-S. Chen and P. C. Burns, *Geology*, 2017, **45**, 1007–1010.
13 R. M. Hazen and A. Navrotsky, *Am. Mineral.*, 1996, **81**, 1021–1035.
14 S. V. Krivovichev, *Mineral. Mag.*, 2013, **77**, 275–326.
15 S. J. McCormack and A. Navrotsky, *Acta Mater.*, 2021, **202**, 1–21.
16 C. M. Rost, E. Sachet, T. Borman, A. Moballegh, E. C. Dickey, D. Hou, J. L. Jones, S. Curtarolo and J.-P. Maria, *Nat. Commun.*, 2015, **6**, 8485.
17 B. Ran, H. Li, R. Cheng, Z. Yang, Y. Zhong, Y. Qin, C. Yang and C. Fu, *Adv. Sci.*, 2024, **11**, 2401034.
18 A. Amiri and R. Shahbazian-Yassar, *J. Mater. Chem. A*, 2021, **9**, 782–823.
19 T. G. Ritter, A. H. Phakatkar, M. G. Rasul, M. T. Saray, L. V. Sorokina, T. Shokuhfar, J. M. Gonçalves and R. Shahbazian-Yassar, *Cell Rep. Phys. Sci.*, 2022, **3**, 100847.

20 S. Zhao, H. Wu, R. Yin, X. Wang, H. Zhong, Q. Fu, W. Wan, T. Cheng, Y. Shi, G. Cai, C. Jiang and F. Ren, *J. Alloys Compd.*, 2021, **868**, 159108.
21 Z. Meng, X. Gong, J. Xu, X. Sun, F. Zeng, Z. Du, Z. Hao, W. Shi, S. Yu, X. Hu and H. Tian, *Chem. Eng. J.*, 2023, **457**, 141242.
22 D. Miracle, J. Miller, O. Senkov, C. Woodward, M. Uchic and J. Tiley, *Entropy*, 2014, **16**, 494–525.
23 J.-W. Yeh, S.-K. Chen, S.-J. Lin, J.-Y. Gan, T.-S. Chin, T.-T. Shun, C.-H. Tsau and S.-Y. Chang, *Adv. Eng. Mater.*, 2004, **6**, 299–303.
24 W. L. Bragg and E. J. Williams, *Proc. R. Soc. London, Ser. A*, 1935, **151**, 540–566.
25 R. DeHoff, *Thermodynamics in Materials Science*, CRC Press, 2nd edn, 2006.
26 Y. Zhong, H. Sabarou, X. Yan, M. Yang, M. C. Gao, X. Liu and R. D. Sisson, *Mater. Des.*, 2019, **182**, 108060.
27 H. L. Tuller and S. R. Bishop, *Annu. Rev. Mater. Res.*, 2011, **41**, 369–398.
28 J. Frenkel, *Z. Phys.*, 1926, **35**, 652–669.
29 W. Schottky, *Z. Phys. Chem.*, 1935, **29B**, 335–355.
30 J. W. E. Drewitt, L. Hennet and D. R. Neuville, *Rev. Mineral. Geochem.*, 2022, **87**, 55–103.
31 A. C. Wright, *J. Non-Cryst. Solids*, 1994, **179**, 84–115.
32 M. A. Halcrow, *Chem. Soc. Rev.*, 2013, **42**, 1784–1795.
33 H. A. Jahn and E. Teller, *Proc. R. Soc. London, Ser. A*, 1937, **161**, 220–235.
34 W. Skubida, D. Jaworski, A. Mielewczyk-Gryń, S. Wachowski, T. Miruszewski, K. Cichy, K. Świerczek and M. Gazda, *J. Phys. Chem. C*, 2023, **127**, 14534–14544.
35 Y. Guan, G. Zhou, Y. Jiang, J. Dong, L. Li, J. Yin, S. Huang, L. Zhang and E. H. Ang, *Sep. Purif. Technol.*, 2025, **358**, 130267.
36 F. Wang, P. Zou, Y. Zhang, W. Pan, Y. Li, L. Liang, C. Chen, H. Liu and S. Zheng, *Nat. Commun.*, 2023, **14**, 6019.
37 J.-W. Yeh, *Ann. Chim. Sci. Mater.*, 2006, **31**, 633–648.
38 G. R. Bejger, M. K. Caucci, S. S. I. Almishal, B. Yang, J.-P. Maria, S. B. Sinnott and C. M. Rost, *arXiv*, 2025, preprint, arXiv.2505.08055, DOI: 10.48550/ARXIV.2505.08055.
39 M. Jankousky, H. Chen, A. Novick and V. Stevanović, *J. Am. Chem. Soc.*, 2024, **146**, 23004–23011.
40 S. S. I. Almishal, L. Miao, Y. Tan, G. N. Kotsonis, J. T. Sivak, N. Alem, L. Chen, V. H. Crespi, I. Dabo, C. M. Rost, S. B. Sinnott and J. Maria, *J. Am. Ceram. Soc.*, 2025, **108**, e20223.
41 G. E. Niculescu, G. R. Bejger, J. P. Barber, J. T. Wright, S. S. I. Almishal, M. Webb, S. V. G. Ayyagari, J.-P. Maria, N. Alem, J. T. Heron and C. M. Rost, *J. Am. Ceram. Soc.*, 2025, **108**, e20171.
42 S. S. I. Almishal, P. Kezer, Y. Iwabuchi, J. T. Sivak, S. V. G. Ayyagari, S. Sarker, M. Furst, G. Bejger, B. Yang, S. Gelin, N. Alem, I. Dabo, C. M. Rost, S. B. Sinnott, V. Crespi, V. Gopalan, R. Engel-Herbert, J. T. Heron and J.-P. Maria, *arXiv*, 2025, preprint, arXiv.2501.09193, DOI: 10.48550/ARXIV.2501.09193.
43 A. R. Mazza, E. Skoropata, Y. Sharma, J. Lapano, T. W. Heitmann, B. L. Musico, V. Keppens, Z. Gai, J. W. Freeland, T. R. Charlton, M. Brahlek, A. Moreo, E. Dagotto and T. Z. Ward, *Adv. Sci.*, 2022, **9**, 2200391.
44 Z. R. Mansley, C. Huang, J. Luo, P. Barry, A. Rodriguez-Campos, M. F. Millares, Z. Wang, L. Ma, S. N. Ehrlich, E. S. Takeuchi, A. C. Marschilok, S. Yan, K. J. Takeuchi and Y. Zhu, *Nano Lett.*, 2024, **24**, 8495–8501.
45 O. F. Dippo, N. Mesgarzadeh, T. J. Harrington, G. D. Schrader and K. S. Vecchio, *Sci. Rep.*, 2020, **10**, 21288.
46 Z. Du, C. Wu, Y. Chen, Q. Zhu, Y. Cui, H. Wang, Y. Zhang, X. Chen, J. Shang, B. Li, W. Chen, C. Liu and S. Yang, *Adv. Energy Mater.*, 2022, **12**, 2103228.
47 P. Edalati, X.-F. Shen, M. Watanabe, T. Ishihara, M. Arita, M. Fuji and K. Edalati, *J. Mater. Chem. A*, 2021, **9**, 15076–15086.
48 H. Johnston, A. P. Black, P. Kayser, J. Oró-Solé, D. A. Keen, A. Fuertes and J. P. Attfield, *Chem. Commun.*, 2018, **54**, 5245–5247.
49 S. Ma, J. Ma, Z. Yang, Y. Gong, K. Li, G. Yu and Z. Xue, *Int. J. Refract. Met. Hard Mater.*, 2021, **94**, 105390.
50 Z. Peng, W. Sun, X. Xiong, H. Zhang, F. Guo and J. Li, *Corros. Sci.*, 2021, **184**, 109359.
51 Y. Wang, T. Csanádi, H. Zhang, J. Dusza and M. J. Reece, *Acta Mater.*, 2022, **231**, 117887.
52 T. Wen, B. Ye, M. C. Nguyen, M. Ma and Y. Chu, *J. Am. Ceram. Soc.*, 2020, **103**, 6475–6489.
53 P. Zhang, X. Liu, A. Cai, Q. Du, X. Yuan, H. Wang, Y. Wu, S. Jiang and Z. Lu, *Sci. China Mater.*, 2021, **64**, 2037–2044.
54 E. J. Pickering and N. G. Jones, *Int. Mater. Rev.*, 2016, **61**, 183–202.
55 F. Otto, Y. Yang, H. Bei and E. P. George, *Acta Mater.*, 2013, **61**, 2628–2638.
56 D. Bérardan, S. Franger, D. Dragoe, A. K. Meena and N. Dragoe, *Phys. Status Solidi RRL*, 2016, **10**, 328–333.
57 R. Feng, P. K. Liaw, M. C. Gao and M. Widom, *npj Comput. Mater.*, 2017, **3**, 50.
58 M. Fracchia, P. Ghigna, T. Pozzi, U. Anselmi Tamburini, V. Colombo, L. Braglia and P. Torelli, *J. Phys. Chem. Lett.*, 2020, **11**, 3589–3593.
59 C. M. Rost, Z. Rak, D. W. Brenner and J.-P. Maria, *J. Am. Ceram. Soc.*, 2017, **100**, 2732–2738.
60 A. Sarkar, R. Kruk and H. Hahn, *Dalton Trans.*, 2021, **50**, 1973–1982.
61 J. Zhang, J. Yan, S. Calder, Q. Zheng, M. A. McGuire, D. L. Abernathy, Y. Ren, S. H. Lapidus, K. Page, H. Zheng, J. W. Freeland, J. D. Budai and R. P. Hermann, *Chem. Mater.*, 2019, **31**, 3705–3711.
62 D. Berardan, A. K. Meena, S. Franger, C. Herrero and N. Dragoe, *J. Alloys Compd.*, 2017, **704**, 693–700.
63 Z. Rák, J.-P. Maria and D. W. Brenner, *Mater. Lett.*, 2018, **217**, 300–303.
64 M. E. Glicksman, *Diffusion in solids: field theory, solid-state principles, and applications*, Wiley, New York Weinheim, 2000.
65 A. Chroneos, *Appl. Sci.*, 2024, **14**, 5309.
66 Q. Wan, F. Zhang and Y. Xiong, *J. Eur. Ceram. Soc.*, 2024, **44**, 6629–6640.

67 Z. Zhao, H. Xiang, F.-Z. Dai, Z. Peng and Y. Zhou, *J. Mater. Sci. Technol.*, 2019, **35**, 2647–2651.
68 J. Dąbrowa, M. Zajusz, W. Kucza, G. Cieślak, K. Berent, T. Czeppe, T. Kulik and M. Danielewski, *J. Alloys Compd.*, 2019, **783**, 193–207.
69 J. Dąbrowa and M. Danielewski, *Metals*, 2020, **10**, 347.
70 S. V. Divinski, A. V. Pokoev, N. Esakkiraja and A. Paul, *Diffus. Found.*, 2018, **17**, 69–104.
71 M. Vaidya, K. G. Pradeep, B. S. Murty, G. Wilde and S. V. Divinski, *Sci. Rep.*, 2017, **7**, 12293.
72 Z. Grzesik, G. Smoła, M. Stygar, J. Dąbrowa, M. Zajusz, K. Mroczka and M. Danielewski, *J. Eur. Ceram. Soc.*, 2019, **39**, 4292–4298.
73 Z. Grzesik, G. Smoła, M. Miszczak, M. Stygar, J. Dąbrowa, M. Zajusz, K. Świerczek and M. Danielewski, *J. Eur. Ceram. Soc.*, 2020, **40**, 835–839.
74 S. Ranganathan, *Curr. Sci.*, 2017, **112**, 1587.
75 X. Zhang, X. Wang and X. Lv, *ChemSusChem*, 2025, **18**, e202401663.
76 J. Hao, F. Ma, Y. Chen, S. Lu, F. Duan, M. Du, C. Wang, W. Zhang and H. Zhu, *New J. Chem.*, 2024, **48**, 511–514.
77 W.-L. Hsu, C.-W. Tsai, A.-C. Yeh and J.-W. Yeh, *Nat. Rev. Chem.*, 2024, **8**, 471–485.
78 C.-H. Li, H.-W. Lin, H.-Y. T. Chen and H.-Y. Chen, in *High-Entropy Materials: Theory, Experiments, and Applications*, ed. J. Brechtl and P. K. Liaw, Springer International Publishing, Cham, 2021, pp. 355–411.
79 S. S. I. Almishal, J. T. Sivak, G. N. Kotsonis, Y. Tan, M. Furst, D. Srikanth, V. H. Crespi, V. Gopalan, J. T. Heron, L.-Q. Chen, C. M. Rost, S. B. Sinnott and J.-P. Maria, *Acta Mater.*, 2024, **279**, 120289.
80 M. Balcerzak, K. Kawamura, R. Bobrowski, P. Rutkowski and T. Brylewski, *J. Electron. Mater.*, 2019, **48**, 7105–7113.
81 D. Bérardan, S. Franger, A. K. Meena and N. Dragoe, *J. Mater. Chem. A*, 2016, **4**, 9536–9541.
82 M. Biesuz, J. Chen, M. Bortolotti, G. Speranza, V. Esposito and V. M. Sglavo, *J. Mater. Chem. A*, 2022, **10**, 23603–23616.
83 M. Biesuz, L. Spiridigliozzi, G. Dell'Agli, M. Bortolotti and V. M. Sglavo, *J. Mater. Sci.*, 2018, **53**, 8074–8085.
84 J. L. Braun, C. M. Rost, M. Lim, A. Giri, D. H. Olson, G. N. Kotsonis, G. Stan, D. W. Brenner, J.-P. Maria and P. E. Hopkins, *Adv. Mater.*, 2018, **30**, 1805004.
85 H. Chen, J. Fu, P. Zhang, H. Peng, C. W. Abney, K. Jie, X. Liu, M. Chi and S. Dai, *J. Mater. Chem. A*, 2018, **6**, 11129–11133.
86 H. Chen, W. Lin, Z. Zhang, K. Jie, D. R. Mullins, X. Sang, S.-Z. Yang, C. J. Jafta, C. A. Bridges, X. Hu, R. R. Unocic, J. Fu, P. Zhang and S. Dai, *ACS Mater. Lett.*, 2019, **1**, 83–88.
87 H. Chen, N. Qiu, B. Wu, Z. Yang, S. Sun and Y. Wang, *RSC Adv.*, 2019, **9**, 28908–28915.
88 J. Chen, W. Liu, J. Liu, X. Zhang, M. Yuan, Y. Zhao, J. Yan, M. Hou, J. Yan, M. Kunz, N. Tamura, H. Zhang and Z. Yin, *J. Phys. Chem. C*, 2019, **123**, 17735–17744.
89 A. D. Dupuy, X. Wang and J. M. Schoenung, *Mater. Res. Lett.*, 2019, **7**, 60–67.
90 Y. Gu, A. Bao, X. Wang, Y. Chen, L. Dong, X. Liu, H. Pan, Y. Li and X. Qi, *Nanoscale*, 2022, **14**, 515–524.
91 W. Hong, F. Chen, Q. Shen, Y. Han, W. G. Fahrenholtz and L. Zhang, *J. Am. Ceram. Soc.*, 2019, **102**, 2228–2237.
92 M. P. Jimenez-Segura, T. Takayama, D. Bérardan, A. Hoser, M. Reehuis, H. Takagi and N. Dragoe, *Appl. Phys. Lett.*, 2019, **114**, 122401.
93 G. N. Kotsonis, C. M. Rost, D. T. Harris and J.-P. Maria, *MRS Commun.*, 2018, **8**, 1371–1377.
94 M. Lim, Zs Rak, J. L. Braun, C. M. Rost, G. N. Kotsonis, P. E. Hopkins, J.-P. Maria and D. W. Brenner, *J. Appl. Phys.*, 2019, **125**, 055105.
95 Z. Lun, B. Ouyang, D.-H. Kwon, Y. Ha, E. E. Foley, T.-Y. Huang, Z. Cai, H. Kim, M. Balasubramanian, Y. Sun, J. Huang, Y. Tian, H. Kim, B. D. McCloskey, W. Yang, R. J. Clément, H. Ji and G. Ceder, *Nat. Mater.*, 2021, **20**, 214–221.
96 P. B. Meisenheimer, T. J. Kratofil and J. T. Heron, *Sci. Rep.*, 2017, **7**, 13344.
97 P. B. Meisenheimer, L. D. Williams, S. H. Sung, J. Gim, P. Shafer, G. N. Kotsonis, J.-P. Maria, M. Trassin, R. Hovden, E. Kioupakis and J. T. Heron, *Phys. Rev. Mater.*, 2019, **3**, 104420.
98 N. Osenciat, D. Bérardan, D. Dragoe, B. Léridon, S. Holé, A. K. Meena, S. Franger and N. Dragoe, *J. Am. Ceram. Soc.*, 2019, **102**, 6156–6162.
99 Y. Pu, D. Moseley, Z. He, K. C. Pitike, M. E. Manley, J. Yan, V. R. Cooper, V. Mitchell, V. K. Peterson, B. Johannessen, R. P. Hermann and P. Cao, *Sci. Adv.*, 2023, **9**, eadi8809.
100 N. Qiu, H. Chen, Z. Yang, S. Sun, Y. Wang and Y. Cui, *J. Alloys Compd.*, 2019, **777**, 767–774.
101 Z. Rak, C. M. Rost, M. Lim, P. Sarker, C. Toher, S. Curtarolo, J.-P. Maria and D. W. Brenner, *J. Appl. Phys.*, 2016, **120**, 095105.
102 C. M. Rost, Z. Rak, D. W. Brenner and J. Maria, *J. Am. Ceram. Soc.*, 2017, **100**, 2732–2738.
103 C. M. Rost, E. Sachet, T. Borman, A. Moballegh, E. C. Dickey, D. Hou, J. L. Jones, S. Curtarolo and J.-P. Maria, *Nat. Commun.*, 2015, **6**, 8485.
104 A. Sarkar, R. Djenadic, N. J. Usharani, K. P. Sanghvi, V. S. K. Chakravadhanula, A. S. Gandhi, H. Hahn and S. S. Bhattacharya, *J. Eur. Ceram. Soc.*, 2017, **37**, 747–754.
105 A. Sarkar, L. Velasco, D. Wang, Q. Wang, G. Talasila, L. De Biasi, C. Kübel, T. Brezesinski, S. S. Bhattacharya, H. Hahn and B. Breitung, *Nat. Commun.*, 2018, **9**, 3400.
106 Q. Wang, A. Sarkar, Z. Li, Y. Lu, L. Velasco, S. S. Bhattacharya, T. Brezesinski, H. Hahn and B. Breitung, *Electrochem. Commun.*, 2019, **100**, 121–125.
107 Q. Wang, A. Sarkar, D. Wang, L. Velasco, R. Azmi, S. S. Bhattacharya, T. Bergfeldt, A. Düvel, P. Heitjans, T. Brezesinski, H. Hahn and B. Breitung, *Energy Environ. Sci.*, 2019, **12**, 2433–2442.
108 Z.-M. Yang, K. Zhang, N. Qiu, H.-B. Zhang, Y. Wang and J. Chen, *Chin. Phys. B*, 2019, **28**, 046201.
109 J. Zhang, J. Yan, S. Calder, Q. Zheng, M. A. McGuire, D. L. Abernathy, Y. Ren, S. H. Lapidus, K. Page, H. Zheng, J. W. Freeland, J. D. Budai and R. P. Hermann, *Chem. Mater.*, 2019, **31**, 3705–3711.

110 Z. Zhang, S. Yang, X. Hu, H. Xu, H. Peng, M. Liu, B. P. Thapaliya, K. Jie, J. Zhao, J. Liu, H. Chen, Y. Leng, X. Lu, J. Fu, P. Zhang and S. Dai, *Chem. Mater.*, 2019, **31**, 5529–5536.
111 S. Zhou, Y. Sun, T. Gao, J. Liao, S. Zhao and G. Cao, *Angew. Chem.*, 2023, **135**, e202311930.
112 J. Dąbrowa, M. Stygar, A. Mikuła, A. Knapik, K. Mroczka, W. Tejchman, M. Danielewski and M. Martin, *Mater. Lett.*, 2018, **216**, 32–36.
113 A. Mao, F. Quan, H.-Z. Xiang, Z.-G. Zhang, K. Kuramoto and A.-L. Xia, *J. Mol. Struct.*, 2019, **1194**, 11–18.
114 A. Mao, H.-Z. Xiang, Z.-G. Zhang, K. Kuramoto, H. Zhang and Y. Jia, *J. Magn. Magn. Mater.*, 2020, **497**, 165884.
115 B. Musicó, Q. Wright, T. Z. Ward, A. Grutter, E. Arenholz, D. Gilbert, D. Mandrus and V. Keppens, *Phys. Rev. Mater.*, 2019, **3**, 104416.
116 T. X. Nguyen, J. Patra, J.-K. Chang and J.-M. Ting, *J. Mater. Chem. A*, 2020, **8**, 18963–18973.
117 A. Radoń, Ł. Hawełek, D. Łukowiec, J. Kubacki and P. Włodarczyk, *Sci. Rep.*, 2019, **9**, 20078.
118 M. Stygar, J. Dąbrowa, M. Moździerz, M. Zajusz, W. Skubida, K. Mroczka, K. Berent, K. Świerczek and M. Danielewski, *J. Eur. Ceram. Soc.*, 2020, **40**, 1644–1650.
119 D. Wang, Z. Liu, S. Du, Y. Zhang, H. Li, Z. Xiao, W. Chen, R. Chen, Y. Wang, Y. Zou and S. Wang, *J. Mater. Chem. A*, 2019, **7**, 24211–24216.
120 M. Biesuz, S. Fu, J. Dong, A. Jiang, D. Ke, Q. Xu, D. Zhu, M. Bortolotti, M. J. Reece, C. Hu and S. Grasso, *J. Australas. Ceram. Soc.*, 2019, **7**, 127–132.
121 S. Jiang, T. Hu, J. Gild, N. Zhou, J. Nie, M. Qin, T. Harrington, K. Vecchio and J. Luo, *Scr. Mater.*, 2018, **142**, 116–120.
122 F. Okejiri, Z. Zhang, J. Liu, M. Liu, S. Yang and S. Dai, *ChemSusChem*, 2020, **13**, 111–115.
123 R. K. Patel, S. K. Ojha, S. Kumar, A. Saha, P. Mandal, J. W. Freeland and S. Middey, *Appl. Phys. Lett.*, 2020, **116**, 071601.
124 Y. Pu, Q. Zhang, R. Li, M. Chen, X. Du and S. Zhou, *Appl. Phys. Lett.*, 2019, **115**, 223901.
125 A. Sarkar, R. Djenadic, D. Wang, C. Hein, R. Kautenburger, O. Clemens and H. Hahn, *J. Eur. Ceram. Soc.*, 2018, **38**, 2318–2327.
126 Y. Sharma, B. L. Musico, X. Gao, C. Hua, A. F. May, A. Herklotz, A. Rastogi, D. Mandrus, J. Yan, H. N. Lee, M. F. Chisholm, V. Keppens and T. Z. Ward, *Phys. Rev. Mater.*, 2018, **2**, 060404.
127 Y. Sharma, Q. Zheng, A. R. Mazza, E. Skoropata, T. Heitmann, Z. Gai, B. Musico, P. F. Miceli, B. C. Sales, V. Keppens, M. Brahlek and T. Z. Ward, *Phys. Rev. Mater.*, 2020, **4**, 014404.
128 Y. Son, S. Udovenko, S. V. G. Ayyagari, J. P. Barber, K. Nakamura, C. M. Rost, N. Alem and S. Trolier-McKinstry, *Acta Mater.*, 2025, **283**, 120576.
129 R. Witte, A. Sarkar, R. Kruk, B. Eggert, R. A. Brand, H. Wende and H. Hahn, *Phys. Rev. Mater.*, 2019, **3**, 034406.
130 S. Zhou, Y. Pu, Q. Zhang, R. Shi, X. Guo, W. Wang, J. Ji, T. Wei and T. Ouyang, *Ceram. Int.*, 2020, **46**, 7430–7437.
131 M. Anandkumar, S. Bhattacharya and A. S. Deshpande, *RSC Adv.*, 2019, **9**, 26825–26830.
132 K. Chen, X. Pei, L. Tang, H. Cheng, Z. Li, C. Li, X. Zhang and L. An, *J. Eur. Ceram. Soc.*, 2018, **38**, 4161–4164.
133 B. Cheng, H. Lou, A. Sarkar, Z. Zeng, F. Zhang, X. Chen, L. Tan, V. Prakapenka, E. Greenberg, J. Wen, R. Djenadic, H. Hahn and Q. Zeng, *Commun. Chem.*, 2019, **2**, 114.
134 J. Gild, M. Samiee, J. L. Braun, T. Harrington, H. Vega, P. E. Hopkins, K. Vecchio and J. Luo, *J. Eur. Ceram. Soc.*, 2018, **38**, 3578–3584.
135 M. Pianassola, M. Loveday, J. W. McMurray, M. Koschan, C. L. Melcher and M. Zhuravleva, *J. Am. Ceram. Soc.*, 2020, **103**, 2908–2918.
136 V. I. Sachkov, R. A. Nefedov and I. V. Amelichkin, *IOP Conf. Ser.: Mater. Sci. Eng.*, 2019, **597**, 012005.
137 A. Sarkar, C. Loho, L. Velasco, T. Thomas, S. S. Bhattacharya, H. Hahn and R. Djenadic, *Dalton Trans.*, 2017, **46**, 12167–12176.
138 M. Pianassola, M. Loveday, J. W. McMurray, M. Koschan, C. L. Melcher and M. Zhuravleva, *J. Am. Ceram. Soc.*, 2020, **103**, 2908–2918.
139 A. Sarkar, C. Loho, L. Velasco, T. Thomas, S. S. Bhattacharya, H. Hahn and R. Djenadic, *Dalton Trans.*, 2017, **46**, 12167–12176.
140 K. Tseng, Q. Yang, S. J. McCormack and W. M. Kriven, *J. Am. Ceram. Soc.*, 2020, **103**, 569–576.
141 F. Li, L. Zhou, J.-X. Liu, Y. Liang and G.-J. Zhang, *J. Adv. Ceram.*, 2019, **8**, 576–582.
142 K. Ren, Q. Wang, G. Shao, X. Zhao and Y. Wang, *Scr. Mater.*, 2020, **178**, 382–386.
143 Z. Teng, L. Zhu, Y. Tan, S. Zeng, Y. Xia, Y. Wang and H. Zhang, *J. Eur. Ceram. Soc.*, 2020, **40**, 1639–1643.
144 A. J. Wright, Q. Wang, S.-T. Ko, K. M. Chung, R. Chen and J. Luo, *Scr. Mater.*, 2020, **181**, 76–81.
145 K. Zhang, W. Li, J. Zeng, T. Deng, B. Luo, H. Zhang and X. Huang, *J. Alloys Compd.*, 2020, **817**, 153328.
146 Z. Zhao, H. Xiang, F.-Z. Dai, Z. Peng and Y. Zhou, *J. Mater. Sci. Technol.*, 2019, **35**, 2647–2651.
147 V. Dubov, A. Bondarau, D. Lelekova, I. Komendo, G. Malashkevich, V. Kouhar, V. Pustovarov, D. Tavrunov and M. Korzhik, *J. Appl. Phys.*, 2024, **135**, 053104.
148 B. Jiang, K. C. Pitike, D.-Y. Lin, S. C. Purdy, X. Wang, Y. Zhao, Y. Zhang, P. Metz, A. Macias and H. M. Meyer, *APL Mater.*, 2023, **11**, 051104.
149 A. R. Mazza, X. Gao, D. J. Rossi, B. L. Musico, T. W. Valentine, Z. Kennedy, J. Zhang, J. Lapano, V. Keppens, R. G. Moore, M. Brahlek, C. M. Rost and T. Z. Ward, *J. Vac. Sci. Technol., A*, 2021, **40**, 013404.
150 W. Zhang, A. R. Mazza, E. Skoropata, D. Mukherjee, B. Musico, J. Zhang, V. M. Keppens, L. Zhang, K. Kisslinger, E. Stavitski, M. Brahlek, J. W. Freeland, P. Lu and T. Z. Ward, *ACS Nano*, 2020, **14**, 13030–13037.
151 J. Y. Lee and W. Cai, *Front. Coat. Dyes Interface Eng.*, 2024, **2**, DOI: **10.3389/frcdi.2024.1417527**.
152 S. S. Jana and T. Maiti, *Mater. Horiz.*, 2023, **10**, 1848–1855.
153 W. T. Riffe, S. Zare, K. D. Ardrey, V. K. Champagne, M. Milich, K. Lee, M. Jassas, S. Makarem, E. J. Opila,

D. R. Clarke, P. V. Balachandran and P. E. Hopkins, *Nat. Commun.*, 2025, **16**, 3333.
154 M. P. Jimenez-Segura, T. Takayama, D. Bérardan, A. Hoser, M. Reehuis, H. Takagi and N. Dragoe, *Appl. Phys. Lett.*, 2019, **114**, 122401.
155 P. B. Meisenheimer, L. D. Williams, S. H. Sung, J. Gim, P. Shafer, G. N. Kotsonis, J.-P. Maria, M. Trassin, R. Hovden, E. Kioupakis and J. T. Heron, *Phys. Rev. Mater.*, 2019, **3**, 104420.
156 R. Witte, A. Sarkar, L. Velasco, R. Kruk, R. A. Brand, B. Eggert, K. Ollefs, E. Weschke, H. Wende and H. Hahn, *J. Appl. Phys.*, 2020, **127**, 185109.
157 R. Witte, A. Sarkar, R. Kruk, B. Eggert, R. A. Brand, H. Wende and H. Hahn, *Phys. Rev. Mater.*, 2019, **3**, 034406.
158 E. Krysko, L. Min, Y. Wang, N. Zhang, J. P. Barber, G. E. Niculescu, J. T. Wright, F. Li, K. Burrage, M. Matsuda, R. A. Robinson, Q. Zhang, R. Katzbaer, R. Schaak, M. Terrones, C. M. Rost and Z. Mao, *APL Mater.*, 2023, **11**, 101123.
159 L. Min, J. P. Barber, Y. Wang, S. V. Gayathri Ayyagari, G. E. Niculescu, E. Krysko, G. R. Bejger, L. Miao, S. H. Lee, Q. Zhang, N. Alem, C. M. Rost and Z. Mao, *J. Am. Chem. Soc.*, 2024, **146**, 24320–24329.
160 B. Yang, Y. Liu, S. Lan, L. Dou, C.-W. Nan and Y.-H. Lin, *J. Appl. Phys.*, 2023, **133**, 110904.
161 L. Chen, S. Deng, H. Liu, J. Wu, H. Qi and J. Chen, *Nat. Commun.*, 2022, **13**, 3089.
162 O. Elmutasim, A. G. Hussien, A. Sharan, S. AlKhoori, M. A. Vasiliades, I. M. A. Taha, S. Kim, M. Harfouche, A.-H. Emwas, D. H. Anjum, A. M. Efstathiou, C. T. Yavuz, N. Singh and K. Polychronopoulou, *ACS Appl. Mater. Interfaces*, 2024, **16**(18), 23038–23053, DOI: **10.1021/acsami.3c16521**.
163 H. T. N. Hai, T. T. Nguyen, M. Nishibori, T. Ishihara and K. Edalati, *Appl. Catal., B*, 2025, **365**, 124968.
164 E. Krysko, L. Min, Y. Wang, N. Zhang, J. P. Barber, G. E. Niculescu, J. T. Wright, F. Li, K. Burrage, M. Matsuda, R. A. Robinson, Q. Zhang, R. Katzbaer, R. Schaak, M. Terrones, C. M. Rost and Z. Mao, *APL Mater.*, 2023, **11**, 101123.
165 C.-C. Lin, H.-Y. Liu, J.-W. Kang, C.-C. Yang, C.-H. Li, H.-Y. T. Chen, S.-C. Huang, C.-S. Ni, Y.-C. Chuang, B.-H. Chen, C.-K. Chang and H.-Y. Chen, *Energy Storage Mater.*, 2022, **51**, 159–171.
166 O. J. Marques, C. Chen, E. V. Timofeeva and C. U. Segre, *J. Power Sources*, 2023, **564**, 232852.
167 O. J. Marques and C. U. Segre, *J. Appl. Phys.*, 2024, **135**, 225001.
168 A. R. Mazza, X. Gao, D. J. Rossi, B. L. Musico, T. W. Valentine, Z. Kennedy, J. Zhang, J. Lapano, V. Keppens, R. G. Moore, M. Brahlek, C. M. Rost and T. Z. Ward, *J. Vac. Sci. Technol., A*, 2022, **40**, 013404.
169 K. Mori, Y. Shimada, H. Yoshida, Y. Hinuma and H. Yamashita, *ACS Appl. Nano Mater.*, 2024, **7**, 28649–28658.
170 G. E. Niculescu, G. R. Bejger, J. P. Barber, J. T. Wright, S. S. I. Almishal, M. Webb, S. V. G. Ayyagari, J. Maria, N. Alem, J. T. Heron and C. M. Rost, *J. Am. Ceram. Soc.*, 2025, **108**, e20171.
171 V. V. Popov, A. P. Menushenkov, A. A. Yastrebtsev, Y. V. Zubavichus, B. R. Gaynanov, A. A. Ivanov, S. G. Rudakov, M. M. Berdnikova, A. A. Pisarev, E. S. Kulikova, E. V. Khramov, N. A. Kolyshkin, V. N. Khrustalev, I. V. Shchetinin, M. K. Tatmyshevskiy, S. M. Novikov, V. S. Volkov, N. A. Tsarenko, N. V. Ognevskaya and O. N. Seregina, *Ceram. Int.*, 2024, **50**, 5319–5335.
172 W. Rosenberg, S. C. Ness, B. Mishra, C. U. Segre and S. J. McCormack, *Acta Mater.*, 2025, **285**, 120639.
173 C. M. Rost, Z. Rak, D. W. Brenner and J. Maria, *J. Am. Ceram. Soc.*, 2017, **100**, 2732–2738.
174 A. Sarkar, B. Eggert, L. Velasco, X. Mu, J. Lill, K. Ollefs, S. S. Bhattacharya, H. Wende, R. Kruk, R. A. Brand and H. Hahn, *APL Mater.*, 2020, **8**, 051111.
175 Y. Yeh, C. Huang, A. Hou, C. Huang, Y. Lin and W. Wu, *Small*, 2024, **20**, 2307284.
176 J. Yue, F. Xiong, Z. Shadike, X. Gao, J. Chen, L. Pi, Y. Yuan, B. Qu, P. Adamson, L. Ma, Q. Li and P. G. Bruce, *J. Power Sources*, 2025, **627**, 235735.
177 L. Zhang, L. Kuang, L. Zhang, W. Chu, H. Qin, J. Zhang, J. He, H. Ni and H. Chi, *J. Energy Chem.*, 2025, **100**, 309–316.
178 A. Sarkar, B. Eggert, R. Witte, J. Lill, L. Velasco, Q. Wang, J. Sonar, K. Ollefs, S. S. Bhattacharya, R. A. Brand, H. Wende, F. M. F. De Groot, O. Clemens, H. Hahn and R. Kruk, *Acta Mater.*, 2022, **226**, 117581.
179 S. S. Aamlid, S. Mugiraneza, M. U. González-Rivas, G. King, A. M. Hallas and J. Rottler, *Chem. Mater.*, 2024, **36**, 9636–9645.
180 B. Cheng, H. Lou, A. Sarkar, Z. Zeng, F. Zhang, X. Chen, L. Tan, K. Glazyrin, H.-P. Liermann, J. Yan, L. Wang, R. Djenadic, H. Hahn and Q. Zeng, *Mater. Today Adv.*, 2020, **8**, 100102.
181 B. Cheng, H. Lou, A. Sarkar, Z. Zeng, F. Zhang, X. Chen, L. Tan, V. Prakapenka, E. Greenberg, J. Wen, R. Djenadic, H. Hahn and Q. Zeng, *Commun. Chem.*, 2019, **2**, 114.
182 B. Jiang, C. A. Bridges, R. R. Unocic, K. C. Pitike, V. R. Cooper, Y. Zhang, D.-Y. Lin and K. Page, *J. Am. Chem. Soc.*, 2021, **143**, 4193–4204.
183 B. Jiang, K. C. Pitike, D.-Y. Lin, S. C. Purdy, X. Wang, Y. Zhao, Y. Zhang, P. Metz, A. Macias, H. M. Meyer, A. Y. Borisevich, J. Yan, V. R. Cooper, C. A. Bridges and K. Page, *APL Mater.*, 2023, **11**, 051104.
184 P. R. Jothi, W. Liyanage, B. Jiang, S. Paladugu, D. Olds, D. A. Gilbert and K. Page, *Small*, 2022, **18**, 2101323.
185 X. Wang, C. Jorgensen, C. Kons, Y. Zhang, J. Liu, P. Metz, E. Calì, D. Gilbert and K. Page, *Struct. Dyn.*, 2025, **12**, A268–A268.
186 H. Guo, H. Vahidi, H. Kang, S. Shah, M. Xu, T. Aoki, T. J. Rupert, J. Luo, K. L. Gilliard-AbdulAziz and W. J. Bowman, *Appl. Phys. Lett.*, 2024, **124**, 171605.
187 B. Gwalani, R. M. Pohan, J. Lee, B. Lee, R. Banerjee, H. J. Ryu and S. H. Hong, *Sci. Rep.*, 2018, **8**, 14085.
188 S. Hanabata, K. Kusada, T. Yamamoto, T. Toriyama, S. Matsumura, S. Kawaguchi, Y. Kubota, Y. Nishida,

M. Haneda and H. Kitagawa, *J. Am. Chem. Soc.*, 2024, **146**, 181–186.
189 Z. Huang, L. Wang, T. Li, K. Venkatraman, Y. He, F. Polo-Garzon, J. Smith, Y. Du, L. Hu, Z. Wu, D. Jiang and M. Chi, *Nano Lett.*, 2024, **24**, 11537–11543.
190 L. Miao, J. T. Sivak, G. Kotsonis, J. Ciston, C. L. Ophus, I. Dabo, J.-P. Maria, S. B. Sinnott and N. Alem, *ACS Nano*, 2024, **18**, 14968–14977.
191 G. E. Niculescu, G. R. Bejger, J. P. Barber, J. T. Wright, S. S. I. Almishal, M. Webb, S. V. G. Ayyagari, J. Maria, N. Alem, J. T. Heron and C. M. Rost, *J. Am. Ceram. Soc.*, 2025, **108**, e20171.
192 A. Ostovari Moghaddam, S. Mehrabi-Kalajahi, X. Qi, R. Salari, R. Fereidonnejad, A. Abdollahzadeh, D. A. Uchaev, E. A. Kazakova, M. A. Varfolomeev, A. Cabot, A. S. Vasenko and E. A. Trofimov, *J. Phys. Chem. Lett.*, 2024, **15**, 7577–7583.
193 S. J. Percival, P. Lu, D. R. Lowry and T. M. Nenoff, *Langmuir*, 2022, **38**, 1923–1928.
194 L. Su, H. Huyan, A. Sarkar, W. Gao, X. Yan, C. Addiego, R. Kruk, H. Hahn and X. Pan, *Nat. Commun.*, 2022, **13**, 2358.
195 J. Tsai, J. Chen, C. Huang, H. Lo, W. Ke, Y. Chu and W. Wu, *Adv. Mater.*, 2023, **35**, 2302979.
196 P. Y. Wu, K. T. Le, H.-Y. Lin, Y.-C. Chen, P.-H. Wu and J. M. Wu, *ACS Nano*, 2023, **17**, 17417–17426.
197 Y. Yeh, C. Huang, A. Hou, C. Huang, Y. Lin and W. Wu, *Small*, 2024, **20**, 2307284.
198 Y. Son, S. Udovenko, S. V. G. Ayyagari, J. P. Barber, K. Nakamura, C. M. Rost, N. Alem and S. Trolier-McKinstry, *Acta Mater.*, 2025, **283**, 120576.
199 C.-Y. Huang, C.-W. Huang, M.-C. Wu, J. Patra, T. Xuyen Nguyen, M.-T. Chang, O. Clemens, J.-M. Ting, J. Li, J.-K. Chang and W.-W. Wu, *Chem. Eng. J.*, 2021, **420**, 129838.
200 L. Miao, J. T. Sivak, G. Kotsonis, J. Ciston, C. L. Ophus, I. Dabo, J.-P. Maria, S. B. Sinnott and N. Alem, *ACS Nano*, 2024, **18**, 14968–14977.
201 A. Sarkar, B. Eggert, L. Velasco, X. Mu, J. Lill, K. Ollefs, S. S. Bhattacharya, H. Wende, R. Kruk, R. A. Brand and H. Hahn, *APL Mater.*, 2020, **8**, 051111.
202 L. Su, J. Ren, T. Lu, K. Chen, J. Ouyang, Y. Zhang, X. Zhu, L. Wang, H. Min, W. Luo, Z. Sun, Q. Zhang, Y. Wu, L. Sun, L. Mai and F. Xu, *Adv. Mater.*, 2023, **35**, 2205751.
203 J. Tsai, J. Chen, C. Huang, H. Lo, W. Ke, Y. Chu and W. Wu, *Adv. Mater.*, 2023, **35**, 2302979.
204 Y. Yeh, C. Huang, A. Hou, C. Huang, Y. Lin and W. Wu, *Small*, 2024, **20**, 2307284.
205 S. V. G. Ayyagari, L. Miao, M. Webb, J. Heron and N. Alem, *Microsc. Microanal.*, 2023, **29**, 1768–1769.
206 L. Miao, G. Kotsonis, J.-P. Maria and N. Alem, *Microsc. Microanal.*, 2020, **26**, 1196–1197.
207 L. Miao, G. Kotsonis, J. Ciston, C. Ophus, J.-P. Maria and N. Alem, *Microsc. Microanal.*, 2021, **27**, 352–354.
208 A. Phakatkar, R. Shahbazian-Yassar and T. Shokuhfar, *Microsc. Microanal.*, 2021, **27**, 884–886.
209 M. R. Chellali, A. Sarkar, S. H. Nandam, S. S. Bhattacharya, B. Breitung, H. Hahn and L. Velasco, *Scr. Mater.*, 2019, **166**, 58–63.
210 A. D. Dupuy, M. R. Chellali, H. Hahn and J. M. Schoenung, *J. Eur. Ceram. Soc.*, 2021, **41**, 4850–4858.
211 A. D. Dupuy, M. R. Chellali, H. Hahn and J. M. Schoenung, *J. Mater. Res.*, 2023, **38**, 198–214.
212 B. Gwalani, R. M. Pohan, J. Lee, B. Lee, R. Banerjee, H. J. Ryu and S. H. Hong, *Sci. Rep.*, 2018, **8**, 14085.
213 D. R. Diercks, G. Brennecka, B. P. Gorman, C. M. Rost and J.-P. Maria, *Microsc. Microanal.*, 2017, **23**, 1640–1641.
214 J. Cieslak, M. Reissner, K. Berent, J. Dabrowa, M. Stygar, M. Mozdzierz and M. Zajusz, *Acta Mater.*, 2021, **206**, 116600.
215 L. Eiselt, R. Kruk, H. Hahn and A. Sarkar, *Int. J. Appl. Ceram. Technol.*, 2023, **20**, 213–223.
216 L. Lin, K. Wang, R. Azmi, J. Wang, A. Sarkar, M. Botros, S. Najib, Y. Cui, D. Stenzel, P. Anitha Sukkurji, Q. Wang, H. Hahn, S. Schweidler and B. Breitung, *J. Mater. Sci.*, 2020, **55**, 16879–16889.
217 S. Mehrabi-Kalajahi, A. Ostovari Moghaddam, F. Hadavimoghaddam, R. Salari, M. A. Varfolomeev, A. L. Zinnatullin, K. R. Minnebaev, D. A. Emelianov, D. A. Uchaev, R. Fereidonnejad, O. Zaitseva, G. R. Khasanova, E. A. Trofimov, A. Rozhenko, A. Cabot and F. G. Vagizov, *ACS Appl. Nano Mater.*, 2024, **7**, 5513–5524.
218 O. Porodko, L. Kavan, M. Fabián, B. Pitňa Lásková, V. Šepelák, H. Kolev, K. L. Da Silva, M. Lisnichuk and M. Zukalová, *Nanoscale*, 2025, **17**, 3739–3751.
219 A. Sarkar, B. Eggert, R. Witte, J. Lill, L. Velasco, Q. Wang, J. Sonar, K. Ollefs, S. S. Bhattacharya, R. A. Brand, H. Wende, F. M. F. De Groot, O. Clemens, H. Hahn and R. Kruk, *Acta Mater.*, 2022, **226**, 117581.
220 G. D. S. Vasconcelos, R. A. Raimundo, M. J. S. Lima, K. F. Galvão, M. D. Da Silva, D. A. Macedo, M. M. Karimi, R. C. Huaman, P. L. Gastelois, U. U. Gomes and M. A. Morales, *J. Alloys Compd.*, 2025, **1022**, 179776.
221 J. Wang, Y. Cui, Q. Wang, K. Wang, X. Huang, D. Stenzel, A. Sarkar, R. Azmi, T. Bergfeldt, S. S. Bhattacharya, R. Kruk, H. Hahn, S. Schweidler, T. Brezesinski and B. Breitung, *Sci. Rep.*, 2020, **10**, 18430.
222 R. Witte, A. Sarkar, L. Velasco, R. Kruk, R. A. Brand, B. Eggert, K. Ollefs, E. Weschke, H. Wende and H. Hahn, *J. Appl. Phys.*, 2020, **127**, 185109.
223 L. Spiridigliozzi, G. Dell'Agli, E. Callone, S. Dirè, R. Campostrini, P. Bettotti, M. Bortolotti, G. Speranza, V. M. Sglavo and M. Biesuz, *J. Alloys Compd.*, 2022, **927**, 166933.
224 D. Z. Tsydypylov, A. B. Slobodyuk, M. A. Kirsanova and N. V. Kosova, *J. Solid State Electrochem.*, 2025, **29**, 2733–2748.
225 J. Chahal, R. Shukla, N. Kumar, R. Dawar, S. Narang, J. Bahadur and V. Grover, *Inorg. Chem.*, 2025, **64**(21), 10513–10525.
226 B. Cheng, H. Lou, A. Sarkar, Z. Zeng, F. Zhang, X. Chen, L. Tan, V. Prakapenka, E. Greenberg, J. Wen, R. Djenadic, H. Hahn and Q. Zeng, *Commun. Chem.*, 2019, **2**, 114.
227 E. Krysko, L. Min, Y. Wang, N. Zhang, J. P. Barber, G. E. Niculescu, J. T. Wright, F. Li, K. Burrage, M. Matsuda, R. A. Robinson, Q. Zhang, R. Katzbaer,

R. Schaak, M. Terrones, C. M. Rost and Z. Mao, *APL Mater.*, 2023, **11**, 101123.
228 V. V. Popov, A. P. Menushenkov, A. A. Yastrebtsev, Y. V. Zubavichus, B. R. Gaynanov, A. A. Ivanov, S. G. Rudakov, M. M. Berdnikova, A. A. Pisarev, E. S. Kulikova, E. V. Khramov, N. A. Kolyshkin, V. N. Khrustalev, I. V. Shchetinin, M. K. Tatmyshevskiy, S. M. Novikov, V. S. Volkov, N. A. Tsarenko, N. V. Ognevskaya and O. N. Seregina, *Ceram. Int.*, 2024, **50**, 5319–5335.
229 Y. Sharma, M.-C. Lee, K. C. Pitike, K. K. Mishra, Q. Zheng, X. Gao, B. L. Musico, A. R. Mazza, R. S. Katiyar, V. Keppens, M. Brahlek, D. A. Yarotski, R. P. Prasankumar, A. Chen, V. R. Cooper and T. Z. Ward, *ACS Appl. Mater. Interfaces*, 2022, **14**, 11962–11970.
230 N. J. Usharani, A. Bhandarkar, S. Subramanian and S. S. Bhattacharya, *Acta Mater.*, 2020, **200**, 526–536.
231 P. Zhang, Z. Lou, L. Gong, J. Xu, Q. Chen, M. J. Reece, H. Yan, Z. Dashevsky and F. Gao, *J. Alloys Compd.*, 2023, **937**, 168366.
232 Z. Zheng, N. Sun, X. He, B. Deng, C.-W. Pao, W.-H. Huang, H. Liu, R. Wang, R. Yu, M. Lei and K. Huang, *J. Alloys Compd.*, 2025, **1032**, 181112.
233 Y. Liu, J. Yang, S. Deng, Y. Zhang, Y. Zhang, S. Sun, L. Wang, X. Jiang, C. Huo, H. Liu, H. Qi, S. Liu and J. Chen, *Acta Mater.*, 2022, **236**, 118115.
234 A. Sarkar, C. Loho, L. Velasco, T. Thomas, S. S. Bhattacharya, H. Hahn and R. Djenadic, *Dalton Trans.*, 2017, **46**, 12167–12176.
235 I. Arcon, B. Mirtic and A. Kodre, *J. Am. Ceram. Soc.*, 1998, **81**, 222–224.
236 F. de Groot, G. Vankó and P. Glatzel, *J. Phys.: Condens. Matter*, 2009, **21**, 104207.
237 S. Calvin, *XAFS for Everyone*, CRC Press, Boca Raton, 2013.
238 B. Ravel and M. Newville, *J. Synchrotron Radiat.*, 2005, **12**, 537–541.
239 M. Newville, *J. Phys.: Conf. Ser.*, 2013, **430**, 012007.
240 G. E. Niculescu, G. R. Bejger, J. P. Barber, J. T. Wright, S. S. I. Almishal, M. Webb, S. V. G. Ayyagari, J.-P. Maria, N. Alem, J. T. Heron and C. M. Rost, *arXiv*, 2024, preprint, arXiv:2406.13550, DOI: **10.48550/arXiv.2406.13550**.
241 M. Fracchia, M. Manzoli, U. Anselmi-Tamburini and P. Ghigna, *Scr. Mater.*, 2020, **188**, 26–31.
242 L. Min, J. P. Barber, Y. Wang, S. V. Gayathri Ayyagari, G. E. Niculescu, E. Krysko, G. R. Bejger, L. Miao, S. H. Lee, Q. Zhang, N. Alem, C. M. Rost and Z. Mao, *J. Am. Chem. Soc.*, 2024, **146**, 24320–24329.
243 G. Van Der Laan and A. I. Figueroa, *Coord. Chem. Rev.*, 2014, **277–278**, 95–129.
244 B. T. Thole, P. Carra, F. Sette and G. Van Der Laan, *Phys. Rev. Lett.*, 1992, **68**, 1943–1946.
245 J. Stöhr and H. König, *Phys. Rev. Lett.*, 1995, **75**, 3748–3751.
246 B. Regmi, D. Miertschin, M. Cocconcelli, F. Stramaglia, D. Crater, L. Yao, C. Piamonteze, S. Van Dijken and A. Farhan, *AIP Adv.*, 2024, **14**, 025023.
247 B. Regmi, M. Cocconcelli, D. Miertschin, D. P. Salinas, G. Panchal, P. Kandel, K. Pandey, I. Ogunniranye, R. Mueller, L. Yao, M. Valvidares, S. Van Dijken and A. Farhan, *J. Magn. Magn. Mater.*, 2025, **613**, 172673.
248 W. Ke, J. Chen, C. Liu, Y. Ku, C. Chang, P. Shafer, S. Lin, M. Chu, Y. Chen, J. Yeh, C. Kuo and Y. Chu, *Adv. Funct. Mater.*, 2024, **34**, 2312856.
249 G. H. J. Johnstone, M. U. González-Rivas, K. M. Taddei, R. Sutarto, G. A. Sawatzky, R. J. Green, M. Oudah and A. M. Hallas, *J. Am. Chem. Soc.*, 2022, **144**, 20590–20600.
250 G. Keresztury, in *Handbook of Vibrational Spectroscopy*, ed. J. M. Chalmers and P. R. Griffiths, Wiley, 1st edn, 2001.
251 *Raman Spectroscopy: Theory and Practice*, ed. H. A. Szymanski, Springer, US, Boston, MA, 1967.
252 J. Dąbrowa, M. Stygar, A. Mikuła, A. Knapik, K. Mroczka, W. Tejchman, M. Danielewski and M. Martin, *Mater. Lett.*, 2018, **216**, 32–36.
253 A. Kirsch, E. D. Bøjesen, N. Lefeld, R. Larsen, J. K. Mathiesen, S. L. Skjærvø, R. K. Pittkowski, D. Sheptyakov and K. M. Ø. Jensen, *Chem. Mater.*, 2023, **35**, 8664–8674.
254 B. Cheng, H. Lou, A. Sarkar, Z. Zeng, F. Zhang, X. Chen, L. Tan, V. Prakapenka, E. Greenberg, J. Wen, R. Djenadic, H. Hahn and Q. Zeng, *Commun. Chem.*, 2019, **2**, 1–9.
255 R. F. Egerton, *Electron Energy-Loss Spectroscopy in the Electron Microscope*, Springer, US, Boston, MA, 2011.
256 A. Sarkar, B. Eggert, L. Velasco, X. Mu, J. Lill, K. Ollefs, S. S. Bhattacharya, H. Wende, R. Kruk, R. A. Brand and H. Hahn, *APL Mater.*, 2020, **8**, 051111.
257 S. V. G. Ayyagari, L. Miao, M. Webb, J. Heron and N. Alem, *Microsc. Microanal.*, 2023, **29**, 1768–1769.
258 A. Phakatkar, R. Shahbazian-Yassar and T. Shokuhfar, *Microsc. Microanal.*, 2021, **27**, 884–886.
259 M. V. Kante, M. L. Weber, S. Ni, I. C. G. van den Bosch, E. van der Minne, L. Heymann, L. J. Falling, N. Gauquelin, M. Tsvetanova, D. M. Cunha, G. Koster, F. Gunkel, S. Nemšák, H. Hahn, L. Velasco Estrada and C. Baeumer, *ACS Nano*, 2023, **17**, 5329–5339.
260 J. Baek, M. D. Hossain, P. Mukherjee, J. Lee, K. T. Winther, J. Leem, Y. Jiang, W. C. Chueh, M. Bajdich and X. Zheng, *Nat. Commun.*, 2023, **14**, 5936.
261 R. L. Mössbauer, *Science*, 1962, **137**, 731–738.
262 *Mössbauer Spectroscopy: Tutorial Book*, ed. Y. Yoshida and G. Langouche, Springer, Berlin, Heidelberg, 2013.
263 Mössbauer Spectroscopy Group, **https://www.rsc.org/membership-and-community/connect-with-others/through-interests/interest-groups/mossbauer/**, (accessed May 29, 2025).
264 P. A. Penczek, *Methods Enzymol.*, 2010, **482**, 73–100.
265 D. B. Williams and C. B. Carter, in *Transmission Electron Microscopy: A Textbook for Materials Science*, ed. D. B. Williams and C. B. Carter, Springer, US, Boston, MA, 2009, pp. 3–22.
266 Transmission electron microscopy (TEM), **https://chem.libretexts.org/Courses/Franklin_and_Marshall_College/Introduction_to_Materials_Characterization__CHM_412_Collaborative_Text/Electron_and_Probe_Microscopy/Transmission_electron_microscopy_(TEM)%3A_TEM_versus_STEM_and_HAADF**, (accessed January 9, 2025).
267 L. Su, H. Huyan, A. Sarkar, W. Gao, X. Yan, C. Addiego, R. Kruk, H. Hahn and X. Pan, *Nat. Commun.*, 2022, **13**, 2358.

268 Z. Huang, L. Wang, T. Li, K. Venkatraman, Y. He, F. Polo-Garzon, J. Smith, Y. Du, L. Hu, Z. Wu, D. Jiang and M. Chi, *Nano Lett.*, 2024, **24**, 11537–11543.
269 Y. Tan, J. T. Sivak, S. S. I. Almishal, J.-P. Maria, S. B. Sinnott, Y. Ji and L.-Q. Chen, *Acta Mater.*, 2025, **286**, 120721.
270 H. Chen, K. Jie, C. J. Jafta, Z. Yang, S. Yao, M. Liu, Z. Zhang, J. Liu, M. Chi, J. Fu and S. Dai, *Appl. Catal., B*, 2020, **276**, 119155.
271 H. Guo, H. Vahidi, H. Kang, S. Shah, M. Xu, T. Aoki, T. J. Rupert, J. Luo, K. Leslie Gilliard-AbdulAziz and W. J. Bowman, *Microsc. Microanal.*, 2024, **30**, ozae044.664.
272 B. Jiang, C. A. Bridges, R. R. Unocic, K. C. Pitike, V. R. Cooper, Y. Zhang, D.-Y. Lin and K. Page, *J. Am. Chem. Soc.*, 2021, **143**, 4193–4204.
273 P. Zhang, Z. Lou, M. Qin, J. Xu, J. Zhu, Z. Shi, Q. Chen, M. J. Reece, H. Yan and F. Gao, *J. Mater. Sci. Technol.*, 2022, **97**, 182–189.
274 B. Gault, A. Chiaramonti, O. Cojocaru-Mirédin, P. Stender, R. Dubosq, C. Freysoldt, S. K. Makineni, T. Li, M. Moody and J. M. Cairney, *Nat. Rev. Methods Primers*, 2021, **1**, 51.
275 M. T. Dove and G. Li, *Nucl. Anal.*, 2022, **1**, 100037.
276 T. Egami and S. J. L. Billinge, *Underneath the Bragg peaks: structural analysis of complex materials*, Pergamon, Kiddington, Oxford, UK Boston, 2003.
277 W. Langel, *ChemTexts*, 2023, **9**, 12.
278 T. Yamaguchi, in *Metal Ions and Complexes in Solution*, ed. T. Yamaguchi and I. Persson, Royal Society of Chemistry, 2023, pp. 20–39.
279 W. G. Stirling, *Complementarity Between Neutron and Synchrotron X-Ray Scattering*, World Scientific, Zuoz, Switzerland, 1998, pp. 87–108.
280 C. L. Farrow, P. Juhas, J. W. Liu, D. Bryndin, E. S. Božin, J. Bloch, T. Proffen and S. J. L. Billinge, *J. Phys.: Condens. Matter*, 2007, **19**, 335219.
281 Y. Zhang, M. Eremenko, V. Krayzman, M. G. Tucker and I. Levin, *J. Appl. Crystallogr.*, 2020, **53**, 1509–1518.
282 P. R. Jothi, W. Liyanage, B. Jiang, S. Paladugu, D. Olds, D. A. Gilbert and K. Page, *Small*, 2022, **18**, 2101323.
283 E. Paquet and H. L. Viktor, *Adv. Chem.*, 2018, **2018**, 1–14.
284 Y. Han, X. Liu, Q. Zhang, M. Huang, Y. Li, W. Pan, P. Zong, L. Li, Z. Yang, Y. Feng, P. Zhang and C. Wan, *Nat. Commun.*, 2022, **13**, 2871.
285 A. Chroneos, *Appl. Sci.*, 2024, **14**, 5309.
286 F.-Z. Dai, B. Wen, Y. Sun, H. Xiang and Y. Zhou, *J. Mater. Sci. Technol.*, 2020, **43**, 168–174.
287 Y. Nomura and R. Akashi, in *Encyclopedia of Condensed Matter Physics*, ed. T. Chakraborty, Academic Press, Oxford, 2nd edn, 2024, pp. 867–878.
288 K. K. Ghose, J. J. Brown, T. J. Frankcombe, A. Page and A. Bayon, *Wiley Interdiscip. Rev.: Energy Environ.*, 2023, **12**, e476.
289 P. Tukur, F. Tukur, Y. Mo, Q. Yan, C. Dun and J. Wei, *Next Mater.*, 2024, **3**, 100192.
290 K. L. Svane and J. Rossmeisl, *Angew. Chem., Int. Ed.*, 2022, **61**, e202201146.
291 C.-C. Lin, C.-W. Chang, C.-C. Kaun and Y.-H. Su, *Crystals*, 2021, **11**, 1035.
292 S. Chae, L. Williams, J. Lee, J. T. Heron and E. Kioupakis, *npj Comput. Mater.*, 2022, **8**, 95.
293 K. C. Pitike, S. KC, M. Eisenbach, C. A. Bridges and V. R. Cooper, *Chem. Mater.*, 2020, **32**, 7507–7515.
294 Monte Carlo Simulation – an overview|ScienceDirect Topics, **https://www.sciencedirect.com/topics/economics-econometrics-and-finance/monte-carlo-simulation**, (accessed January 12, 2025).
295 A. R. Mazza, E. Skoropata, Y. Sharma, J. Lapano, T. W. Heitmann, B. L. Musico, V. Keppens, Z. Gai, J. W. Freeland, T. R. Charlton, M. Brahlek, A. Moreo, E. Dagotto and T. Z. Ward, *Adv. Sci.*, 2022, **9**, 2200391.
296 A. V. Motseyko and N. V. Ter-Oganessian, *J. Alloys Compd.*, 2024, **976**, 172945.
297 L. Min, J. P. Barber, Y. Wang, S. V. Gayathri Ayyagari, G. E. Niculescu, E. Krysko, G. R. Bejger, L. Miao, S. H. Lee, Q. Zhang, N. Alem, C. M. Rost and Z. Mao, *J. Am. Chem. Soc.*, 2024, **146**, 24320–24329.
298 B. Ravel, in *X-Ray Absorption and X-Ray Emission Spectroscopy*, ed. J. A. Van Bokhoven and C. Lamberti, John Wiley & Sons, Ltd, Chichester, UK, 2016, pp. 281–302.
299 B. Jiang, C. A. Bridges, R. R. Unocic, K. C. Pitike, V. R. Cooper, Y. Zhang, D.-Y. Lin and K. Page, *J. Am. Chem. Soc.*, 2021, **143**, 4193–4204.
300 M. T. Dove, M. G. Tucker and D. A. Keen, *Eur. J. Mineral.*, 2002, **14**, 331–348.
301 M. Zhang, X. Duan, Y. Gao, S. Zhang, X. Lu, K. Luo, J. Ye, X. Wang, Q. Niu, P. Zhang and S. Dai, *ACS Appl. Mater. Interfaces*, 2023, **15**, 45774–45789.
302 M. G. Tucker, D. A. Keen, M. T. Dove, A. L. Goodwin and Q. Hui, *J. Phys.: Condens. Matter*, 2007, **19**, 335218.
303 C. M. Rost, E. Sachet, T. Borman, A. Moballegh, E. C. Dickey, D. Hou, J. L. Jones, S. Curtarolo and J.-P. Maria, *Nat. Commun.*, 2015, **6**, 8485.
304 D. Bérardan, S. Franger, A. K. Meena and N. Dragoe, *J. Mater. Chem. A*, 2016, **4**, 9536–9541.
305 A. Sarkar, L. Velasco, D. Wang, Q. Wang, G. Talasila, L. De Biasi, C. Kübel, T. Brezesinski, S. S. Bhattacharya, H. Hahn and B. Breitung, *Nat. Commun.*, 2018, **9**, 3400.